8-2013

# Investigation of Sound Transmission through an Open Window into a Room

Caleb F. Sieck
*University of Nebraska-Lincoln*, cfsieck@gmail.com

# INVESTIGATION OF SOUND TRANSMISSION THROUGH AN OPEN WINDOW INTO A ROOM

by

Caleb Frederick Sieck

A THESIS

Presented to the Faculty of

The Graduate College at the University of Nebraska

In Partial Fulfillment of Requirements

For the Degree of Master of Science

Major: Architectural Engineering

Under the Supervision of Professor Siu-Kit Lau

Lincoln, Nebraska

August, 2013

# INVESTIGATION OF SOUND TRANSMISSION THROUGH AN OPEN WINDOW INTO A ROOM

Caleb Frederick Sieck, M.S.

University of Nebraska, 2013

Advisor: Siu-Kit Lau

In recent decades, noise levels in cities and the associated annoyance and health consequences have become regular topics of discussion. As a result, the assessment of environmental noise transmitting into buildings has received much attention. Current models of sound transmission through open windows have either neglected their thickness or the presence of a room behind on one side. The objectives of the present work were to (1) develop an accurate analytical model of sound transmission through an open window of finite thickness into a room, (2) verify the analytical model using a finite element model and experimental measurements, and (3) to express the various regions of the model in terms of impedance matrices. The motivation behind the third objective is that active noise control design based on the impedance-mobility approach has shown much promise, and the mathematical combination of impedance matrices representing two distinct regions linked by a finite aperture has not been considered. To better understand the mechanics by which sound transmits through the window, the present investigation developed an analytical model of a baffled rectangular aperture of finite thickness backed by a rigid walled cavity. The effect of aperture thickness on the insertion loss and sound pressure levels inside the cavity was studied with the analytical model, which was validated by a finite element model of the system. Increasing window

thickness decreases the amount of sound transmitted at frequencies below the (1,1) mode of the cavity. Using the impedance-mobility approach, the model can be extended to consider many noise control treatments to windows including active noise control.

## Acknowledgements

To my family and friends, my advisor Dr. Siu-Kit Lau, and my committee members Dr. Lily Wang and Dr. Yaoqing Yang, thank you for all your advice, support, and never-ending encouragement.

# Table of Contents

## List of Figures

# Chapter 1 – Introduction

## 1.1 Motivation

In recent decades, noise levels in cities and the associated annoyance and health consequences have become regular topics of discussion (Amundsen et al., 2013; de Araújo and Bistafa, 2012; Naish et al., 2012; Kluizenaar et al., 2011). As a result, the assessment of environmental noise transmitting into buildings has received much attention, such as vehicle noise prediction methods (Asakura et al., 2013; Steele, 2001) and development of standards to evaluate the effectiveness of façades and windows at mitigating this noise (Buratti et al., 2013; Berardi, 2012; Sánchez Bote et al., 2012). As with any noise-related issue, three approaches can be taken: controlling the noise at the source, in the transmission, or at the receiver (Bies and Hansen, 2009). For the problem of noise transmission into buildings, controlling the transmission is often the most reasonable option. The best approach to reducing the noise transmission is to fortify the weakest element, which for building façades are normally windows, especially when they are open as is common in warmer climates.

The objectives of the present work were to (1) develop an accurate analytical model of sound transmission through an open window of finite thickness into a room, (2) verify the analytical model using a finite element model and experimental measurements, and (3) to express the various regions of the model in terms of impedance matrices that are compatible with the mobility and impedance methods of structural dynamics used in the analysis of structural-acoustic systems (Gardonio and Brennan, 2002; Kim and

Brennan, 1999). The motivation behind the third objective is that active noise control design based on the impedance-mobility approach has shown much promise (Lau, 2003; Lau and Tang, 2001), and the mathematical combination of impedance matrices representing two distinct regions linked by a finite aperture has not been considered, e.g. an open window of finite thickness connecting a room to some other environment.

## 1.2 Literature Review

A literature review on apertures was conducted to understand the propagation of sound through open windows, and previous research on cavities was considered for the derivation of the sound field in a room. As the following development depends on modal analysis of the various regions (exterior, window/aperture, and room/cavity), studies related to duct acoustics are also relevant, as apertures may be analyzed as short ducts and cavities can be considered terminated ducts.

### 1.2.1 Sound transmission into a cavity

Previous research has considered the propagation of sound into cavities but treated the apertures as an open wall and neglected the finite thickness of the aperture (Jean, 2009; Zhang et al., 2002; Kropp and Berillon, 1998). Studies of sound propagating into a cavity have used the geometry pictured in Figure 1.1 consisting of a cavity with an opening $S$ and thickness $d = 0$ in an infinite rigid baffle. At $S$, incident, reflected, and radiated waves are coupled to modes in the cavity.

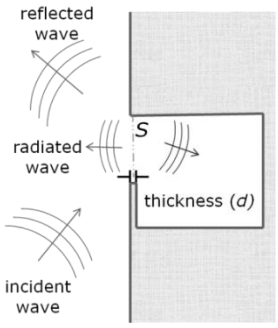


**Figure 1.1 – Sound transmission into a cavity (Sieck and Lau, 2011)**

Zhang et al. (2002) studied the coherence of acoustic pressure on either side of a window due to traffic noise. Results from his theoretical evaluation were well-matched to results from in-situ experiments indicating that it is reasonable to model noise control techniques for this situation. The focus of two other studies (Jean, 2009; Kropp and Berillon, 1998) was to model the sound field within an external balcony and propose techniques to decrease sound levels. At low and middle frequencies there were higher sound pressure levels at the back of the balcony due to resonance modes. Because the wall between a balcony and the interior of a building is often comprised of glass, which acts as a low pass filter, there would be an increase in sound transmission into the building at low and middle frequencies. Recent research has looked at more specifically at balcony design to reflect environmental noise (Ishizuka and Fujiwara, 2012) and the associated health benefits (Naish et al., 2012).

### 1.2.2 Sound transmission through apertures of finite thickness

Several studies have analyzed the radiation and transmission of sound by an aperture of finite thickness set in a rigid, infinite baffle with the sound as arriving from

and propagating into semi-infinite regions (Sgard et al., 2007; Horner and Peat, 2006; Pierce et al., 2002; Sauter, Jr. and Soroka, 1970). The radiation from an aperture is of particular interest because it is the most computationally difficult. Several approximations and numerical solutions have been proposed (Horner and Peat, 2006; Nelisse et al., 1998; Park and Eom, 1997), and an analytic solution has been developed by Pierce et al. (2002) for an aperture backed by an arbitrary acoustic system. Sauter, Jr. and Soroka (1970) developed a theoretical relationship for the transmission of sound between two reverberant rooms, and Sgard et al. (2007) developed a mathematical model for an aperture bounded on both sides by half-space. Experimental validation for this model was provided by Trompette et al. (2009). As shown in Figure 1.2, this model consisted of incident, reflected, and radiated waves existing in half-space coupled to aperture modes through the surface $S_1$; the aperture modes were then coupled to a wave radiating into a second half-space through surface $S_2$.

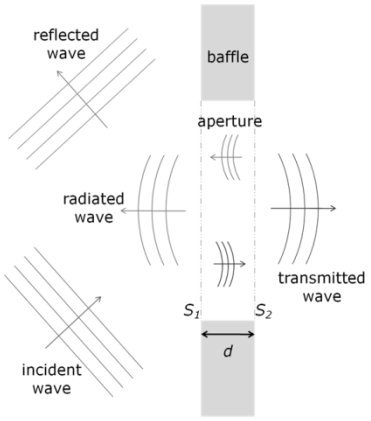


**Figure 1.2 – Sound transmission through an aperture (Sieck and Lau, 2011)**

### 1.2.3 Active noise control and the impedance-mobility approach

One method that has been investigated to control sound in the systems introduced in the two previous sections is that of active noise control, generating sound to cancel out sound. This approach is particularly attractive because it works with the window open, thereby allowing airflow. Active systems have been proposed for sound transmission through an aperture in a rigid screen (Emms and Fox, 2001; Duhamel and Sergent, 1998), a transparent acoustic transducer as a window to cancel external noise but not internal sound (Hu et al., 2013), and an active window system for an open window with sensors exterior to the building and control sources on the window frame (Kwon and Park, 2013).

The impedance-mobility approach was originally developed to study structural dynamics (Gardonio and Brennan, 2002), and has been recently been applied to the analysis of coupled structural-acoustic systems (Kim and Brennan, 1999). Lau and Tang (2001) used this approach to develop an active noise control system for structure-borne noise in a cavity. They showed that with this approach, the energy-density in a cavity can be significantly reduced.

## 1.3 Thesis Outline

Chapter 2 provides a description of the present model of a finite aperture backed by a cavity and contains the mathematical development to analytically model the sound fields. The details regarding simulations of the analytical model and finite element model and the experiment are contained in Chapter 3, and the results and discussion of these

studies are presented in Chapter 4. An impedance-mobility expression of the analytical model is developed in Chapter 5.

# Chapter 2 – Theoretical Development

## 2.1 Introduction

### 2.1.1 Geometry of the model

The geometry under consideration in this thesis is shown in Figure 2.1. The geometry consists of a cavity with dimensions $L_x \times L_y \times L_z$ with an opening in the $xy$ plane notated in Figure 2.1 as $S_2$. The aperture between surfaces $S_1$ and $S_2$ has some finite thickness, $d$, and beyond surface $S_1$ in the negative z-direction is infinite half-space.

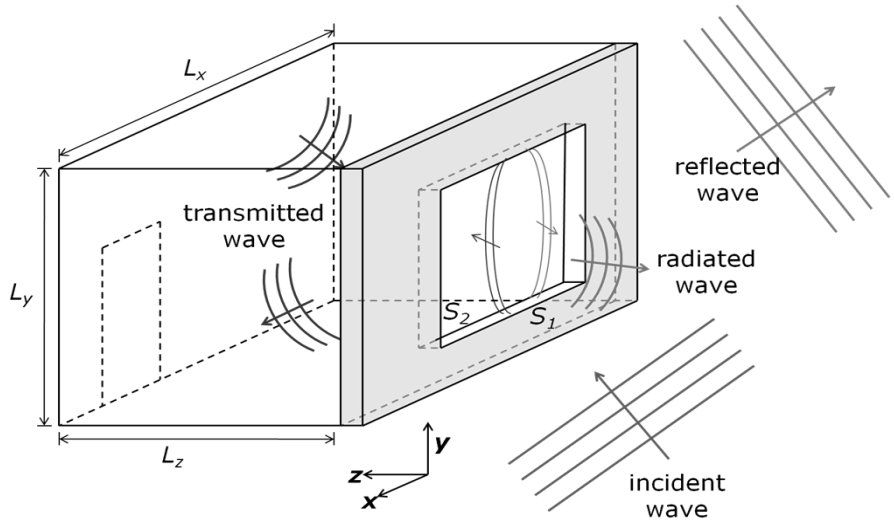


**Figure 2.1 – Present model of sound transmission into a cavity through an aperture of finite thickness (Sieck and Lau, 2011)**

The coordinate systems and dimensions are displayed in Figure 2.2 which shows cuts along the planes $x = 0$ and $y = 0$. The origin is centered on $S_1$, and this opening extends $-a < x < a$ and $-b < y < b$. For generality, the aperture (i.e. the opening) may

not be centered on the cavity wall. Lengths $a_1$, $b_1$, $a_2$, and $b_2$ were defined such that $a_1$ and $b_1$ are the distances from the aperture to the cavity walls in the negative $x$ and $y$ directions, respectively, and $a_2$ and $b_2$ are the distances from the origin to the cavity walls in the positive $x$ and $y$ directions, respectively.

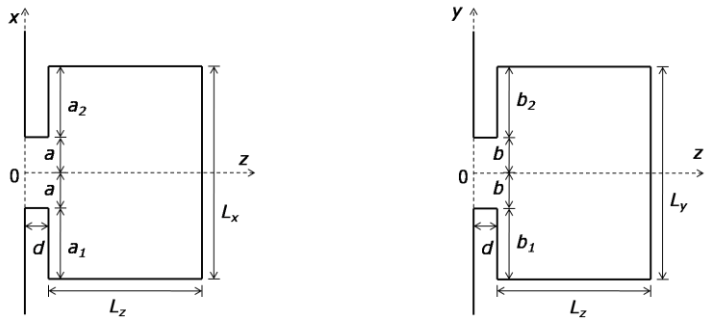


**Figure 2.2 – Coordinate system and dimensions of present model**

The goal is to model the half-space, aperture, and cavity as acoustic and/or mechanical impedances such that the impedance-mobility approach (Kim and Brennan, 1999) can be used to model noise control treatments, such as active control (Lau and Tang, 2001). There are three "impedance" terms that appear in the study of acoustics: mechanical impedance which maps a velocity to a force potential, specific acoustic impedance which maps particle velocity to acoustic pressure, and acoustic impedance which maps volume velocity to acoustic pressure (Kinsler et al., 2000). The following development will be performed in terms of mechanical and acoustic impedances. Certainly specific acoustic impedance could be used as well; see, for example, Muehleisen (1996). However, in the interest of making the results compatible with the

impedance-mobility method, all impedances will be reported as mechanical or acoustic. The impedance-mobility method is addressed in Chapter 5.

### 2.1.2 Notation

Assuming a continuous, time-harmonic, acoustic pressure field, the following development will be presented in the frequency domain using the time convention in Equation (2.1) where $\omega$ denotes the angular frequency of the sound, $t$ is time, and $p$ is the complex amplitude of acoustic pressure. Variables will be subscripted with either an $a$ for aperture or $c$ for cavity, and impedances will be superscripted with an $M$ for mechanical or $A$ for acoustic.

$$\hat{p}(x, y, z, t) = p(x, y, z)e^{j\omega t} \tag{2.1}$$

## 2.2 Regional Development

### 2.2.1 Sound field in half-space

The half-space region, $z \leq 0$, can be replaced by an interface boundary condition written as the sum of an incident wave, reflected wave, and a wave radiated from the aperture: $p_{int} = p_{inc} + p_{re} + p_{rad}$. According to the method of images, the reflected wave will have the same form as the incident wave except that the argument $z$ is replaced by its negative (Kinsler et al., 2000). The surface boundary condition dictates the combination of incident and reflected on the surface $z = 0$, here assumed to be rigid except on the aperture. The outward normal component (away from surface and into half-space) of the particle velocity at $z = 0$, $u_n(x, y, 0)$, where the subscript *n* denotes surface

normal, will be zero everywhere except possibly on the aperture, a result of assuming rigid boundary conditions. Because there is non-zero particle velocity on the aperture, it can be regarded as the source of the wave that radiates from the aperture into half-space (Pierce et al., 2002). Therefore, the acoustic pressure on the interface of the aperture and the half-space region can be written as

$$p_{int}(x, y, 0) = 2p_{inc}(x, y, 0) + p_{rad}(x, y, 0), \tag{2.2}$$

where the incident and reflected waves constructively interfere on the surface and the radiated acoustic pressure is given by the Rayleigh integral,

$$p_{rad}(x, y, 0) = j\omega\rho \int_{S_a'} G_{rad}(x, y, 0|x', y', 0) u_n(x', y', 0)\, dS_a' \tag{2.3}$$

(Sgard et al., 2007; Pierce et al., 2002; Zhang et al., 2002). Here, $G_{rad}(x, y, 0|x', y', 0) = e^{-jkR}/2\pi R$ is the Green's function for radiation from an aperture in a rigid baffle, and $R = \sqrt{(x - x')^2 + (y - y')^2}$ is the distance between two points on the surface $z = 0$.

The incident acoustic pressure wave can be generated by any source in the half-space. Particular sources considered in the literature include an incident plane wave (Sgard et al., 2007), a point source (Jean, 2009; Kropp and Berillon, 1998), and an incoherent line source to model traffic flow (Zhang et al., 2002; Duhamel and Sergent, 1998).

2.2.2 Sound field in aperture

Equation (2.4) expresses the acoustic pressure within the aperture, notated by the subscript *a*, using a Fourier expansion of propagating and evanescent modes along the *z*-axis (Sgard et al., 2007).

$$p_a(x,y,z) = \sum_{mn} \phi_{a,mn}(x,y)\left[e^{-jk_{a,mn}(z-d)}P^{+}_{a,mn} + e^{jk_{a,mn}(z-d)}P^{-}_{a,mn}\right] \tag{2.4}$$

$P^{+}_{a,mn}$ and $P^{-}_{a,mn}$ are pressure amplitudes of the $mn$ mode for waves traveling in the $\pm z$ directions where subscripts $m$ and $n$ are mode identifiers in the $x$ and $y$ directions, respectively. The modal wavenumbers are represented by $k_{a,mn}$, while $\phi_{a,mn}(x,y)$ are the transverse mode shapes for the aperture modeled as a rectangular waveguide.

The transverse mode shapes for a rectangular waveguide with rigid walls and dimensions $2a \times 2b$ can be written as

$$\phi_{a,mn}(x,y) = \sqrt{(2-\delta_{m0})(2-\delta_{0n})}\cos\left[\frac{m\pi}{2a}(x+a)\right]\cos\left[\frac{n\pi}{2b}(y+b)\right], \tag{2.5}$$

and by orthogonality

$$\int_{S_a} \phi_{a,mn}(x,y)\phi_{a,\xi\eta}(x,y)\,dS_a = A_a\delta_{mn,\xi\eta} = 4ab\delta_{mn,\xi\eta}, \tag{2.6}$$

where $\delta_{mn,\xi\eta} = \delta_{m\xi}\delta_{n\eta}$ and $\delta_{m\xi} = \begin{cases} 1, m = \xi \\ 0, m \neq \xi \end{cases}$ in Equations (2.5) and (2.6) is the Dirac delta function. From the transverse modes, the wavenumber in the $+z$ direction can be expressed as

$$k_{a,mn} = \begin{cases} \sqrt{k^2 - \left(\frac{m\pi}{2a}\right)^2 - \left(\frac{n\pi}{2b}\right)^2}; \text{ propagating modes} \\ -j\sqrt{\left(\frac{m\pi}{2a}\right)^2 + \left(\frac{n\pi}{2b}\right)^2 - k^2}; \text{ evanescent modes} \end{cases} \tag{2.7}$$

where $k = 2\pi/\lambda$ is the acoustic wavenumber in free space and the expression under the radical is real and positive. The z-component of the particle velocity, Equation (2.8), in the aperture can be calculated from the linear Euler's equation (Kinsler et al., 2000), $\partial p_a/\partial z = -j\omega\rho u_a$, for the time-harmonic assumption, where $\rho$ is the mass density of the fluid in the aperture. In Equation (2.8), the particle velocity has been written in terms of the modal phase velocity, which is related to the wavenumber by $c_{a,mn} = \omega/k_{a,mn}$, which is either purely real or purely imaginary.

$$\begin{aligned} u_a(x,y,z) &= \sum_{mn} \phi_{a,mn}(x,y) \frac{1}{\rho c_{a,mn}} \left[e^{-jk_{a,mn}(z-d)} P_{a,mn}^{+} - e^{jk_{a,mn}(z-d)} P_{a,mn}^{-}\right] \\ &= \sum_{mn} \phi_{a,mn}(x,y) U_{a,mn}(z) \end{aligned} \tag{2.8}$$

2.2.3 Sound field in cavity

In the same manner as the aperture, the acoustic field within the cavity, indicated by subscript *c*, was expanded analytically in terms of propagating and evanescent modes along the *z*-axis. By solving for the rigid boundary conditions, at the back of the cavity, $z = L_z + d$, and around the aperture,

$$\left.\frac{\partial p_c}{\partial x}\right|_{x=\begin{cases} a+a_2 \\ -a-a_1 \end{cases}} = \left.\frac{\partial p_c}{\partial y}\right|_{y=\begin{cases} b+b_2 \\ -b-b_1 \end{cases}} = \left.\frac{\partial p_c}{\partial z}\right|_{z=L_z+d} = 0, \tag{2.9}$$

the acoustic pressure everywhere in the cavity can be expressed as

$$p_c(x,y,z) = \sum_{rs} \phi_{c,rs}(x,y) \cos\left[k_{c,rs}(L_z + d - z)\right] P_{c,rs} \tag{2.10}$$

where $P_{c,rs}$ is the pressure amplitude in the cavity for the $rs$ mode, and the wavenumber in the cavity is given in Equation (2.11).

$$k_{c,rs} = \sqrt{k^2 - \left(\frac{r\pi}{L_x}\right)^2 - \left(\frac{s\pi}{L_y}\right)^2}. \tag{2.11}$$

Transverse mode shapes are given by Equation (2.12), and as in the aperture development, the orthogonality condition and particle velocity are expressed in Equations

(2.13) and (2.14), respectively. Re-expressing Equation (2.14) with tangent and cosine functions rather than sine aids in combining the aperture and cavity equations at the boundary, and it also makes taking the low frequency limit more intuitive.

$$\phi_{c,rs}(x,y) = \sqrt{(2-\delta_{r0})(2-\delta_{0s})}\cos\left[\frac{r\pi}{L_x}(a+a_2-x)\right]\cos\left[\frac{s\pi}{L_y}(b+b_2-y)\right] \tag{2.12}$$

$$\int_{S_c} \phi_{c,rs}(x,y)\phi_{c,\xi\eta}(x,y)\,dS_c = A_c\delta_{rs,\xi\eta} = L_xL_y\delta_{rs,\xi\eta} \tag{2.13}$$

$$\begin{aligned} u_c(x,y,z) &= \sum_{rs}\phi_{c,rs}(x,y)\frac{-1}{j\rho c_{c,rs}}\sin\left[k_{c,rs}(L_z+d-z)\right]P_{c,rs} \\ &= \sum_{rs}\phi_{c,rs}(x,y)\frac{j\tan\left[k_{c,rs}(L_z+d-z)\right]}{\rho c_{c,rs}}\cos\left[k_{c,rs}(L_z+d-z)\right]P_{c,rs} \end{aligned} \tag{2.14}$$

## 2.3 Solving Boundary Conditions

From now on, aperture modes will always be labeled as $mn$ or $\xi\eta$, and cavity modes will be labeled $rs$. For all three of the mode identifying pairs, the first letter corresponds to the $x$ dimension, and the second corresponds to the $y$ dimension.

### 2.3.1 Development of modal radiation matrix

The boundary conditions on surface $S_1$, the interface between the aperture and half-space ($-a < x < a$, $-b < y < b$ and $z = 0$), are continuity of acoustic pressure, $p_{int}|_{z=0} = p_a|_{z=0}$, and continuity of normal velocity, $\frac{\partial p_{rad}}{\partial z}|_{z=0} = \frac{\partial p_a}{\partial z}|_{z=0}$. From

continuity of particle velocity, $u_n$ in Equation (2.3) can be replaced with $-u_a$ as in Equation (2.15). The surface $S_1$ has area $A_a$, the cross-sectional area of the aperture.

$$p_{rad}(x,y,0) = j\omega\rho \int_{S_1'} G_{rad}(x,y,0|x',y',0)[-u_a(x',y',0)]\, dS_1' \tag{2.15}$$

Equation (2.16) is obtained from continuity of pressure and Equation (2.17) is the result of substituting the Green's function and the expression for $u_a$ into the Rayleigh integral.

$$\sum_{mn} \phi_{a,mn}(x,y)\left[e^{jk_{a,mn}d}P_{a,mn}^{+} + e^{-jk_{a,mn}d}P_{a,mn}^{-}\right] = 2p_{inc}(x,y,0) - j\omega\rho \int_{S_1'} G_{rad}(x,y,0|x',y',0)u_a(x',y',0)\, dS_1' \tag{2.16}$$

$$\begin{aligned}\sum_{mn} \phi_{a,mn}(x,y)\left[e^{jk_{a,mn}d}P_{a,mn}^{+} + e^{-jk_{a,mn}d}P_{a,mn}^{-}\right] &= 2p_{inc}(x,y,0) - j\omega\rho \int_{S_1'} \frac{e^{-jkR}}{2\pi R} \sum_{mn} \phi_{a,mn}(x',y') \frac{1}{\rho c_{a,mn}} \left[e^{jk_{a,mn}d}P_{a,mn}^{+} - e^{-jk_{a,mn}d}P_{a,mn}^{-}\right] dS_1' \\ &= 2p_{inc}(x,y,0) - j\omega\rho \sum_{mn} \int_{S_1'} \frac{e^{-jkR}}{2\pi R} \phi_{a,mn}(x',y')\, dS_1' \frac{1}{\rho c_{a,mn}} \left[e^{jk_{a,mn}d}P_{a,mn}^{+} - e^{-jk_{a,mn}d}P_{a,mn}^{-}\right]\end{aligned} \tag{2.17}$$

Multiplying Equation (2.17) by $\phi_{a,\xi\eta}$ and integrating over the surface $S_1$ gives:

$$j\omega\rho\sum_{mn}\int_{S_1}\int_{S_1'}\phi_{a,\xi\eta}(x,y)\frac{e^{-jkR}}{2\pi R}\phi_{a,mn}(x',y')\,dS_1'\,dS_1\frac{1}{\rho c_{a,mn}}\left[e^{jk_{a,mn}d}P_{a,mn}^{+}-e^{-jk_{a,mn}d}P_{a,mn}^{-}\right]$$
$$=2\int_{S_1}\phi_{a,\xi\eta}(x,y)p_{inc}(x,y,0)\,dS_1-A_a\left[e^{jk_{a,\xi\eta}d}P_{a,\xi\eta}^{+}+e^{-jk_{a,\xi\eta}d}P_{a,\xi\eta}^{-}\right]. \tag{2.18}$$

Defining the incident force, or source term, as in Equation (2.19) and the mechanical radiation impedance in Equation (2.20), now Equation (2.18) can be expressed as a sum of forces as in Equation (2.21).

$$F_{inc,\xi\eta}=2\int_{S_1}\phi_{a,\xi\eta}(x,y)p_{inc}(x,y,0)\,dS_1 \tag{2.19}$$

$$Z_{\xi\eta,mn}^{M,rad}=j\omega\rho\int_{S_1}\int_{S_1'}\phi_{a,\xi\eta}(x,y)\frac{e^{-jkR}}{2\pi R}\phi_{a,mn}(x',y')\,dS_1'\,dS_1 \tag{2.20}$$

$$A_a\left[e^{jk_{a,\xi\eta}d}P_{a,\xi\eta}^{+}+e^{-jk_{a,\xi\eta}d}P_{a,\xi\eta}^{-}\right]$$
$$=F_{inc,\xi\eta}-\sum_{mn}Z_{\xi\eta,mn}^{M,rad}\frac{1}{\rho c_{a,mn}}\left[e^{jk_{a,mn}d}P_{a,mn}^{+}-e^{-jk_{a,mn}d}P_{a,mn}^{-}\right] \tag{2.21}$$

### 2.3.2 Development of cavity impedance matrix

Applying the same boundary conditions as in the previous section to Equations (2.4), (2.8), (2.10), and (2.14) on the surface $S_2$, the interface between the aperture and the cavity ($-a<x<a$, $-b<y<b$ and $z=d$) also with area $A_a$, produces Equation (2.22) from continuity of pressure and Equation (2.23) from continuity of particle velocity.

$$\sum_{rs} \phi_{c,rs}(x,y)\cos\left[k_{c,rs}L_z\right]P_{c,rs} = \sum_{mn} \phi_{a,mn}(x,y)\left[P^{+}_{a,mn} + P^{-}_{a,mn}\right] \quad \begin{pmatrix}\text{Valid for}\\ -a < x < a\\ -b < y < b\end{pmatrix} \tag{2.22}$$

$$\sum_{rs} \phi_{c,rs}(x,y)\frac{j\tan\left[k_{c,rs}L_z\right]}{\rho c_{c,rs}}\cos\left[k_{c,rs}L_z\right]P_{c,rs} = \sum_{mn} \phi_{a,mn}(x,y)\frac{1}{\rho c_{a,mn}}\left[P^{+}_{a,mn} - P^{-}_{a,mn}\right]H(x,y) \tag{2.23}$$

Here $H(x,y) = h(x+a)h(a-x)h(y+b)h(b-y)$where $h(x)$ is the Heaviside unit step function defined as $h(x) = \begin{cases}0; x < 0\\ 1; x \geq 0\end{cases}$.

Multiplying the continuity of pressure expression, Equation (2.22), by $\phi_{a,\xi\eta}$ and integrating over $S_2$ results in

$$\sum_{rs}\int_{S_2} \phi_{a,\xi\eta}(x,y)\phi_{c,rs}(x,y)\,dS_2\cos\left[k_{c,rs}L_z\right]P_{c,rs} = A_a\left[P^{+}_{a,\xi\eta} + P^{-}_{a,\xi\eta}\right]. \tag{2.24}$$

Similarly, multiplying the particle velocity expression, Equation (2.23), by $\phi_{c,r's'}$ and integrating over $S_c$, the cross-section of the cavity at $z = d$ with area$A_c$, gives

$$\begin{aligned} &A_c\frac{j\tan\left[k_{c,rs}L_z\right]}{\rho c_{c,rs}}\cos\left[k_{c,rs}L_z\right]P_{c,rs}\\ &\qquad = \sum_{mn}\int_{S_2} \phi_{c,rs}(x,y)\phi_{a,mn}(x,y)\,dS_2\frac{1}{\rho c_{a,mn}}\left[P^{+}_{a,mn} - P^{-}_{a,mn}\right], \end{aligned} \tag{2.25}$$

which can be rearranged as

$$\cos[k_{c,rs}L_z]P_{c,rs} = \frac{\rho c_{c,rs}}{jA_c \tan[k_{c,rs}L_z]} \sum_{mn} \int_{S_2} \phi_{c,rs}(x,y)\phi_{a,mn}(x,y)\, dS_2 \frac{1}{\rho c_{a,mn}} [P^+_{a,mn} - P^-_{a,mn}]. \quad (2.26)$$

Equations (2.27) and (2.28) define the coupling coefficients, which map modes of one region to the other. The coupling of cavity modes to aperture modes is presented in Equation (2.27), and Equation (2.28) couples aperture modes to cavity modes. Although, they appear to be the same integral, and analytically they are, numerically they are represented as matrices and are the transpose of one another. The effort to keep these equations separate will become more apparent when they are cast into impedance matrices in Chapter 5.

$$C^{a\leftarrow c}_{\xi\eta,rs} = \int_{S_a} \phi_{a,\xi\eta}(x,y)\phi_{c,rs}(x,y)\, dS_a \quad (2.27)$$

$$C^{c\leftarrow a}_{rs,mn} = \int_{S_a} \phi_{c,rs}(x,y)\phi_{a,mn}(x,y)\, dS_a \quad (2.28)$$

Combining Equations (2.24) and (2.26) to eliminate $P_{c,rs}$ results in the force-velocity relation given by Equation (2.29). Also, the notation in Equations (2.27) and (2.28) makes more sense if Equation (2.29) is worked from right to left as one would for matrix multiplication. Now, the modal impedance of the cavity, as seen by the aperture, can be expressed as in Equation (2.30), which maps aperture modes to aperture modes, notated by the subscript $\xi\eta, mn$, via cavity modes and the coupling coefficients. The superscript $M$ identifies $Z^{M,c}_{\xi\eta,mn}$ as mechanical impedance, and superscript $c$ indicates cavity.

$$A_a\left[P^+_{a,\xi\eta} + P^-_{a,\xi\eta}\right] = \sum_{mn}\sum_{rs} C^{a\leftarrow c}_{\xi\eta,rs} \frac{\rho c_{c,rs}}{jA_c \tan\left[k_{c,rs}L_z\right]} C^{c\leftarrow a}_{rs,mn} \frac{1}{\rho c_{a,mn}} \left[P^+_{a,mn} - P^-_{a,mn}\right]$$
$$= \sum_{mn} Z^{M,c}_{\xi\eta,mn} \frac{1}{\rho c_{a,mn}} \left[P^+_{a,mn} - P^-_{a,mn}\right] \quad (2.29)$$

$$Z^{M,c}_{\xi\eta,mn} = \sum_{rs} C^{a\leftarrow c}_{\xi\eta,rs} \frac{\rho c_{c,rs}}{jA_c \tan\left[k_{c,rs}L_z\right]} C^{c\leftarrow a}_{rs,mn} \quad (2.30)$$

## 2.4 Numerical Implementation

### 2.4.1 Implementation of boundary conditions

With Equations (2.21) and (2.29), we now have sums of forces on surfaces $S_1$ and $S_2$ of the aperture. These equations have been rearranged to show this more clearly in Equations (2.31) and (2.32), respectively. The right-hand-side of Equation (2.31) is the force on $S_1$ due to the incident acoustic wave. This is balanced on the left-hand-side by the force on the surface due to the field in the aperture (i.e. pressure multiplied by area) and the radiated force, particle velocity on the surface multiplied by the radiation impedance. Because there is no source in either the aperture or the cavity, the force at $S_2$ due to the acoustic pressure in the aperture is balanced by that of the particle velocity multiplied by the modal mechanical impedance of the cavity.

$$A_a\left[e^{jk_{a,\xi\eta}d}P^+_{a,\xi\eta} + e^{-jk_{a,\xi\eta}d}P^-_{a,\xi\eta}\right]$$
$$+ \sum_{mn} Z^{M,rad}_{\xi\eta,mn} \frac{1}{\rho c_{a,mn}} \left[e^{jk_{a,mn}d}P^+_{a,mn} - e^{-jk_{a,mn}d}P^-_{a,mn}\right] = F_{inc,\xi\eta} \quad (2.31)$$

$$A_a\left[P_{a,\xi\eta}^{+} + P_{a,\xi\eta}^{-}\right] - \sum_{mn} Z_{\xi\eta,mn}^{M,c} \frac{1}{\rho c_{a,mn}}\left[P_{a,mn}^{+} - P_{a,mn}^{-}\right] = 0 \tag{2.32}$$

The acoustic pressure amplitudes for each mode at a single frequency in the aperture can now be solved for by setting up Equations (2.31) and (2.32) as a system of equations as in Equation (2.33), where $\mathbf{\Psi_i}$ are square matrices whose size is determined by the number of aperture modes kept in the calculation. $P_a^{\pm}$ and $F_{inc}$ are vectors of values for each mode $\xi\eta$. $\mathbf{\Psi_i}$ terms are defined in Equation (2.34).

$$\begin{bmatrix} \mathbf{\Psi_1} & \mathbf{\Psi_2} \\ \mathbf{\Psi_3} & \mathbf{\Psi_4} \end{bmatrix} \begin{bmatrix} P_a^{+} \\ P_a^{-} \end{bmatrix} = \begin{bmatrix} F_{inc} \\ 0 \end{bmatrix} \tag{2.33}$$

$$\begin{aligned} \Psi_{1,\xi\eta,mn} &= A_a e^{jk_{a,\xi\eta}d}\delta_{\xi\eta,mn} + Z_{\xi\eta,mn}^{M,rad}\frac{1}{\rho c_{a,mn}} e^{jk_{a,mn}d} \\ \Psi_{2,\xi\eta,mn} &= A_a e^{-jk_{a,\xi\eta}d}\delta_{\xi\eta,mn} - Z_{\xi\eta,mn}^{M,rad}\frac{1}{\rho c_{a,mn}} e^{-jk_{a,mn}d} \\ \Psi_{3,\xi\eta,mn} &= A_a\delta_{\xi\eta,mn} - Z_{\xi\eta,mn}^{M,c}\frac{1}{\rho c_{a,mn}} \\ \Psi_{4,\xi\eta,mn} &= A_a\delta_{\xi\eta,mn} + Z_{\xi\eta,mn}^{M,c}\frac{1}{\rho c_{a,mn}} \end{aligned} \tag{2.34}$$

### 2.4.2 Calculating insertion loss

In order to quantify the difference in sound level in the cavity for apertures of different cross-sectional areas and depths, the average energy density in the cavity, $AED_c$, was calculated as in Equation (2.35). Here, $V_c$ is the volume of the cavity, and $ED_c$ is the

energy density at every point in the cavity as expressed in Equation (2.36). The average energy density of the incident plane wave is given in Equation (2.37) (Kinsler et al., 2000). Now, the insertion loss of the system can be calculated using Equation (2.38).

$$AED_c = \frac{1}{V_c}\int_{V_c} ED_c \, dV_c \tag{2.35}$$

$$ED_c = \frac{|\hat{p}_c|^2}{2\rho c^2} + \frac{\rho|\nabla\hat{p}_c|^2}{2(\rho c k)^2} \tag{2.36}$$

$$AED_{inc} = \frac{P_{inc}^2}{2\rho_0 c^2} \tag{2.37}$$

$$IL = 10\log_{10}\left(\frac{AED_i}{AED_{rm}}\right) \tag{2.38}$$

## 2.5 Summary

The system of interest, an aperture of finite thickness set in a rigid baffle and backed by a cavity, was established. Using Fourier expansions, the acoustic pressure in the aperture and cavity were modeled, and the half-space was modeled as the sum of incident and reflected plane waves and the wave radiated from the aperture. By solving boundary conditions on surfaces $S_1$ and $S_2$, as defined in Figure 2.1, the system of equations expressed in Equation (2.33) was established to solve for the acoustic pressure amplitudes in the aperture for a single frequency, which in turn can be used to solve for the acoustic variables in all three regions. The average energy density in the cavity can be calculated from the acoustic pressure as in Equation (2.35). Because the average energy

density of a plane wave is known, the insertion loss of the system can be calculated using Equation (2.38). A new system of equations must be generated and solved for each frequency of interest.

# Chapter 3 – Simulation and Experiment

## 3.1 Model Dimensions

Dimensions, as defined in Figure 2.2, were chosen to create model approximately one-fifth the size of an office or bedroom and are presented in Table 3.1. To avoid degenerate acoustic modes in the cavity and aperture (Lau and Tang, 2001), the ratio of cavity dimensions, $L_x$ (width) × $L_y$ (height) × $L_z$ (depth), were chosen such that $L_x : L_y : L_z = 1 : 2/\pi : e/\pi$, and the ratio of transverse aperture dimensions, $2a$ (width) × $2b$ (height), was $a : b = 1 : 5/2\pi$ for both the small and large window. The effect of aperture thickness on the insertion loss into a cavity was investigated using six aperture arrangements. Apertures with the three thicknesses 0.03m (thin), 0.10m (medium), 0.20m (deep) were modeled for two different cross-sectional areas (small and large) as listed in Table 3.1. The large aperture corresponded to 20% of the cavity wall, and the small aperture corresponded to 5% of the wall. To study the effect of thickness on insertion loss, the aperture was intentionally not centered on the wall to guarantee that all cavity modes would be excited by an incident plane wave. Thus, $a_1 \neq a_2$ and $b_1 \neq b_2$, which are defined in Figure 2.2.

**Table 3.1 – Model dimensions**

| Dimensions (m) | $a$ | $a_1$ | $a_2$ | $b$ | $b_1$ | $b_2$ | $d$ | $L_x$ | $L_y$ | $L_z$ |
|---|---|---|---|---|---|---|---|---|---|---|
| Small Aperture | 0.10 | 0.35 | 0.45 | 0.08 | 0.26 | 0.21 | 0.03, 0.10, 0.20 | 1.00 | 0.63 | 0.86 |
| Large Aperture | 0.20 | 0.20 | 0.40 | 0.16 | 0.18 | 0.13 | 0.03, 0.10, 0.20 | 1.00 | 0.63 | 0.86 |

## 3.2 Simulations

### 3.2.1 Analytical model

In all analytical calculations, a slight damping factor of 0.01Np/m was applied to the fluid in the cavity to maintain finite acoustic pressure levels at resonance frequencies.

Low frequency finite element simulations (up to 500Hz) were used to verify the present analytical model and to determine the impact of keeping a finite number of evanescent modes in the cavity and aperture on the insertion loss calculation. For the low frequency studies, the large aperture was used and was centered on the wall in order to excite only the symmetric transverse modes in the aperture and cavity. This aided in verifying the model, which will be discussed in the next section. The source in these studies was a normally incident plane wave. All propagating modes were kept in the simulations.

To determine the number of evanescent modes to be kept in the aperture and cavity for each frequency, the damping factor that would result in the sound pressure level of a wave decaying by a given decibel value (here 0dB, 5dB and 10dB were used) over the thickness of the aperture was calculated. Evanescent modes in the aperture and cavity that had a wavenumber magnitude less than the calculated damping factor were kept in the calculation. Evanescent modes "make non-zero contributions to the mean square pressure averaged over the duct [or in this case aperture and cavity] cross-section, although their contributions to mean acoustic power are all identically zero" (Doak, 1973a). Equation (2.36) calculates the energy density in the cavity from pressure squared

values. Modes that are near cut-on but evanescent can have large enough acoustic pressure values to impact this calculation.

The broadband insertion loss of the aperture-cavity coupled system was calculated numerically using MATLAB for each aperture defined in Table 3.1 from the analytical expressions developed in Chapter 2. To understand the general effect of the aperture thickness up to 2000Hz, the apertures were simulated with radiation boundaries on both sides, which reduced the derived system of equations to that of Sgard et al. (2007). The effect of the aperture becomes apparent when plotted with the response of the present coupled system. For these and the remaining studies, the apertures are not centered on the wall as discussed in Section 3.1.

The frequency response of the system was calculated for an obliquely incident plane wave, 45° from plan and section planes, up to 4400Hz with 2Hz steps from 2Hz to 998Hz, with 5Hz steps from 1000Hz to 3525Hz, and with 10Hz steps from 3530Hz to 4400Hz. One-third octave band sound pressure levels were evaluated from the frequency response at the four microphone positions used in the experiment, as described in Section 3.3. The resulting number of calculation points for each 1/3$^{rd}$ octave band are listed in Table 3.2.

**Table 3.2 – Number of points per 1/3$^{rd}$ octave band**

| 1/3$^{rd}$ octave band (Hz) | 63 | 80 | 100 | 125 | 160 | 200 | 250 | 315 | 400 | 500 |
|---|---|---|---|---|---|---|---|---|---|---|
| Number of points | 7 | 8 | 13 | 14 | 17 | 25 | 29 | 35 | 43 | 63 |
| | | | | | | | | | | |
| 1/3$^{rd}$ octave band (Hz) | 630 | 800 | 1000 | 1250 | 1600 | 2000 | 2500 | 3150 | 4000 | |
| Number of points | 71 | 86 | 86 | 57 | 69 | 98 | 115 | 141 | 87 | |

### 3.2.2 Finite element model

A finite element model (FEM) of the system was developed using the Acoustics Module for COMSOL 4.1 to verify the response calculated by the analytical model at low frequencies. Neither the radiation boundary condition nor the perfectly matched layer approximation in COMSOL could be used due to the non-ideal radiation condition of the aperture, i.e. not a simple plane wave. Therefore, the FEM was used only to verify the situation of a normally incident plane wave. A source waveguide was constructed to guarantee that the acoustic energy entered and exited the system as a plane wave, which also required that the aperture be centered on the cavity wall to prevent asymmetric modes in the waveguide. To avoid exciting the first symmetric mode in the waveguide, this study required two models with source waveguides of different cross-sections in order to maintain only plane waves in the waveguide.

The mesh was constructed such that no element was larger than one-eighth of a wavelength (Herrin and Seybert, 2006). At very low frequencies a realistic model could be made as shown in Figure 3.1a, which consisted of a large source waveguide, 2m long with a square cross-section with 1.5m long sides. To sufficiently verify the analytical model, a smaller source waveguide also had to be used, which had stronger coupling to the cavity and looked less like a half-space, as shown in Figure 3.1b. The smaller source waveguide was 1m long and had a square cross-section with 0.5m sides.

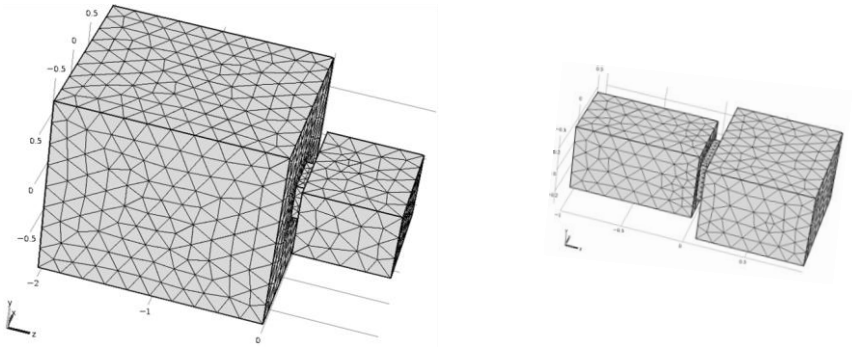

a) b)

**Figure 3.1 – FEM model with the cavity on the right for a) large and b) small source waveguides**

## 3.3 Experiment

### 3.3.1 Equipment

Table 3.3 lists all sound generation and measurement equipment used in the experiment.

### 3.3.2 Setup

A schematic of the experimental setup is presented in Figure 3.2. Stars represent coordinate origins, and two coordinate systems were used, one for the source room and one for the cavity. In Figure 3.2, microphone positions are indicated by dots labeled LD# for Larson Davis 824 sound level meters and BK# for B&K microphone positions; the coordinates of these positions are listed in Tables 3.4 and 3.5, which provides the location of BK2 for all six aperture locations: thin-small (TS), medium-small (MS), deep-small (DS), thin-large (TL), medium-large (ML), and deep-large (DL). The numbers next to the microphone dots indicate the location of the microphone on the out-of-page axis, $x$. Figure 3.3 displays the microphone arrangement in the cavity.

**Table 3.3 – Equipment used in experiment**

| Equipment | Model Number | Description |
|---|---|---|
| Sound Level Meter | Larson Davis 824 | ANSI/IEC Type 1 Sound level meter |
| | Larson Davis PRM902 | General-purpose microphone preamplifier |
| | Larson Davis 2560 | random incidence, ½ inch microphone designed with high sensitivity for low level measurements |
| | Larson Davis CAL200 | Class 1 Sound Calibrator for microphones |
| Signal Generator | Larson Davis SRC20 | Hand-held digital signal generator |
| Omni-directional Sound Source | Provided by Larson Davis | Six-sided loudspeaker assembly |
| Power Amplifier | Lab.gruppen LAB 500 | 500 watt 2-channel power amplifier |
| Data Acquisition System | B&K 3050-A-060 | PULSE data acquisition hardware, multipurpose input/output LAN-XI module with 6-channel input |
| | B&K 4231 | Class 1 and LS sound calibrator for microphones |
| | B&K 2671 | DeltaTron® ½ inch microphone preamplifier |
| | B&K 4189 | Free-field, ½ inch microphone for high precision measurements |

The source room was 2.57m by 3.04m by 3.30m with thin carpet flooring, gypsum walls, a drop ceiling made with acoustical tiles, and an assortment of items being stored that acted as diffusers and additional absorption. The door of the source room was covered by a sheet of 15cm thick plywood, except for the aperture (see insert near aperture in Figure 3.2). Apertures and the cavity were also constructed of 15cm thick plywood. As shown in Figure 3.4, the cavity was placed on rollers for support and to easily move it to and from the door frame to change apertures. The cavity was bolted to the door sheet during measurements to prevent it from rolling away.

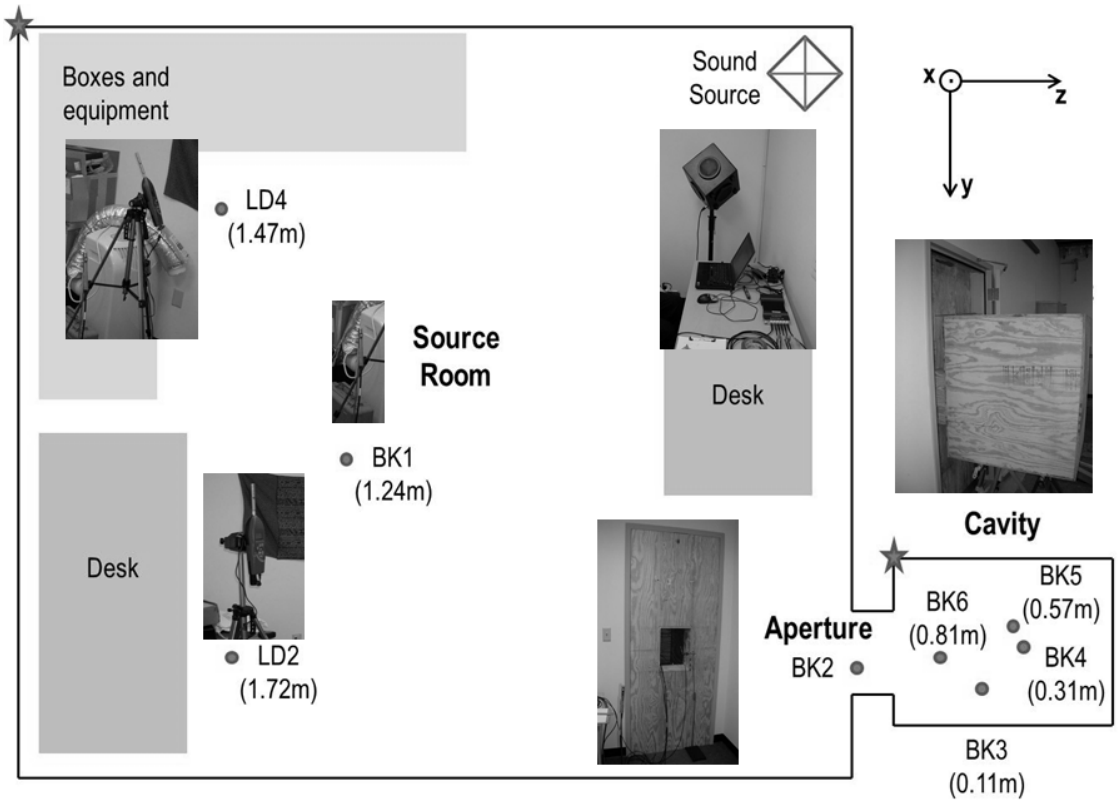


**Figure 3.2 – Experimental setup. Two coordinate systems were used with origins indicated by stars, one for the source room and one for the cavity. Dots labeled BK# and LD# indicate microphone and sound level meter locations, respectively**

**Table 3.4 – Microphone locations in test room and cavity**

| Coordinate system | Microphone | x (m) | y (m) | z (m) |
|---|---|---|---|---|
| Test Room Coordinates | LD2 | 1.72 | 2.54 | 1.38 |
| | LD4 | 1.47 | 0.75 | 1.35 |
| | BK1 | 1.24 | 1.70 | 1.97 |
| | | | | |
| Cavity Coordinates | BK3 | 0.11 | 0.51 | 0.38 |
| | BK4 | 0.31 | 0.34 | 0.58 |
| | BK5 | 0.57 | 0.26 | 0.47 |
| | BK6 | 0.81 | 0.40 | 0.19 |

**Table 3.5 – Microphone BK2 location for each aperture setting and setting identifier**

| | Thin (m) | Medium (m) | Deep (m) |
|---|---|---|---|
| Small | -0.03, 0.04, 0.00 (TS) | -0.04, 0.04, 0.03 (MS) | -0.04, 0.04, 0.04 (DS) |
| Large | 0.02, 0.10, 0.00 (TL) | 0.01, 0.11, 0.03 (ML) | 0.01, 0.08, 0.06 (DL) |

**Figure 3.3 – Microphone setup in cavity**

**Figure 3.4– Cavity connected to test room and sitting on rollers**

### 3.3.3 Procedure

First, all microphones were calibrated. B&K microphones were calibrated to 94 dB (re 20µPa), and Larson Davis SLMs were calibrated to 114dB (re 20µPa). Next, background noise level measurements were taken at all microphone locations. Then, for each insertion loss measurement, the room was excited by approximately 90dB (re 20µPa) of pink noise, and measurements were time averaged over 10s. Each measurement consisted of a fast Fourier transform (FFT) analysis up to 6400Hz with a resolution of 1Hz and a 1/3$^{rd}$ octave band central pass-band (CPB) analysis for each of the six B&K microphones and 1/3$^{rd}$ octave band measures at each Larson Davis SLM. Three measurements were taken for each aperture setting. Figure 3.5 shows the door sheet with three of the aperture inserts, thin/small, deep/small, and deep/large, from left to right, respectively.

**Figure 3.5 – View of aperture and BK2 placement. From left to right, thin/small, deep/small, and deep/large aperture from test room**

### 3.4 Summary

The analytical model derived in Chapter 2 was solved numerically. A finite element model was developed to verify the analytical model at low frequencies, and an experiment was performed to verify the higher frequencies. From low frequency studies (up to 500Hz), the frequencies at which various modes occurred could be verified, and the impact of keeping a finite number of evanescent modes in the cavity and aperture on the insertion loss calculation could be determined. Six apertures were used to study the effect of thickness on insertion loss. Apertures of three different depths were made for two aperture cross-sectional areas. The aperture connected the cavity, all made from plywood, to a source room. Two sound level meters and one measurement microphone were placed in the test room, which was excited by an omni-directional sound source. To measure the effect of the aperture on sound pressure levels in the cavity, four microphones were placed in the cavity and one in the aperture.

# Chapter 4 – Results and Discussion

## 4.1 Verification of Analytical Model

The first fifteen transverse modes for both aperture cross-sections (large and small) and the cavity were calculated using Equations 2.7 and 2.11, respectively, and are presented in Table 4.1. Note that the lowest modes for the large and small apertures are 429Hz and 858Hz, respectively. For frequencies above the first cavity mode and lower than the first aperture mode, transmission was dominated by the response of the cavity and the fluid in the aperture appeared as an entrained mass.

**Table 4.1 – Transverse Modes in the Cavity and Aperture**

| Cavity Modes | | | Large Aperture Modes | | | Small Aperture Modes | | |
|---|---|---|---|---|---|---|---|---|
| **r** | **s** | **Freq. (Hz)** | **m** | **n** | **Freq. (Hz)** | **m** | **n** | **Freq. (Hz)** |
| 1 | 0 | 172 | 1 | 0 | 429 | 1 | 0 | 858 |
| 0 | 1 | 272 | 0 | 1 | 536 | 0 | 1 | 1072 |
| 1 | 1 | 322 | 1 | 1 | 686 | 1 | 1 | 1373 |
| 2 | 0 | 343 | 2 | 0 | 858 | 2 | 0 | 1715 |
| 2 | 1 | 438 | 2 | 1 | 1011 | 2 | 1 | 2022 |
| 3 | 0 | 515 | 0 | 2 | 1072 | 0 | 2 | 2144 |
| 0 | 2 | 544 | 1 | 2 | 1154 | 1 | 2 | 2309 |
| 1 | 2 | 571 | 3 | 0 | 1286 | 3 | 0 | 2573 |
| 3 | 1 | 582 | 2 | 2 | 1373 | 2 | 2 | 2745 |
| 2 | 2 | 643 | 3 | 1 | 1393 | 3 | 1 | 2789 |
| 4 | 0 | 686 | 0 | 3 | 1608 | 0 | 3 | 3216 |
| 4 | 1 | 738 | 1 | 3 | 1664 | 1 | 3 | 3328 |
| 3 | 2 | 749 | 3 | 2 | 1674 | 3 | 2 | 3349 |
| 0 | 3 | 817 | 4 | 0 | 1715 | 4 | 0 | 3430 |
| 1 | 3 | 834 | 4 | 1 | 1797 | 4 | 1 | 3594 |
| 5 | 0 | 858 | 2 | 3 | 1822 | 2 | 3 | 3644 |

### 4.1.1 Model verification by FEM

In Figure 4.1, the present analytical model developed in Chapter 2 is compared to the results of the finite element model (FEM). For this comparison, evanescent modes which decay less than 5dB over the aperture thickness were kept in the analytical model (see Section 3.2.1 for an explanation of how the number of evanescent modes to be kept in the calculation was determined). The present model has very good agreement with the FEM model with the large source waveguide, which as described in Chapter 3, provided a good free space approximation. They both captured the abrupt drop in insertion loss at the Helmholtz resonance of the system at 45Hz, as shown in Figure 4.1. At the Helmholtz resonance, the fluid in the aperture oscillates as an entrained mass in series with the cavity acting as a lumped spring (Kinsler et al., 2000). All models captured the first on axis resonance at 207Hz due to depth of the cavity in series with the thickness of the aperture, which adds apparent distance to the depth of the cavity lowering this resonance frequency.

Due to the requirement that only plane waves propagate in the waveguide, the FEM with the large source waveguide could only be used up to 200Hz. Above this frequency, the present model was compared only to the FEM with the small source waveguide. The next drop in insertion loss was due to the first transverse symmetric mode in the cavity. Both the FEM and present models showed that this occurred at 346Hz, which is very close to the value listed in Table 4.1 of 343Hz. Because the FEM with the small source waveguide did not approximate the half-space as well, it was not

expected to be in exact agreement with the present model; however, it did confirm that the present model was correctly capturing the response of the cavity at low frequencies.

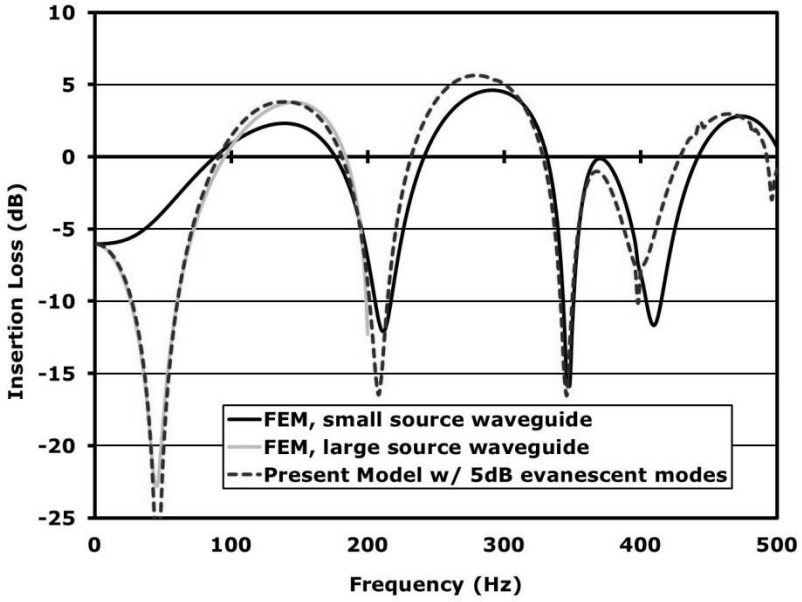


**Figure 4.1 – Comparison of FEM model and present model including some evanescent modes**

### 4.1.2 Effect of evanescent modes on calculations

In Figure 4.1, the number of evanescent modes kept in the present model, those that decayed less than 5dB, resulted in very good agreement with the FEM. In addition to 5dB, the response was calculated for evanescent modes which decayed up to 0dB (i.e. keeping only propagating modes in the calculation) and 10dB, as shown in Figure 4.2. When only the propagating modes were kept in the insertion loss calculation (black solid line), the present model captured the on axis modes of the system but showed extremely steep dips in insertion loss near transverse modal resonances such as at 344Hz. Just before this resonance, keeping only propagation modes in the calculation overestimates

the insertion loss by 5dB. When evanescent modes that decayed up to 10dB over their respective length scales were kept, very strong coupling resulted between some evanescent modes in the aperture and propagating modes in the cavity. A nice example of this occurred at 178Hz, the first asymmetric resonance of the cavity. Because the first asymmetric mode in the aperture was kept in the calculation (although very weak), the first asymmetric mode in the cavity was excited due to strong coupling between these two modes. The excitation of the first asymmetric mode in the cavity is not physically possible since the system was driven symmetrically, as was verified by the FEM (Figure 4.1). One can predict that if many more modes had been used in the calculation, this anomaly would be canceled out. As a result of this study, evanescent modes that decayed up to 5dB were kept in the remaining calculations.

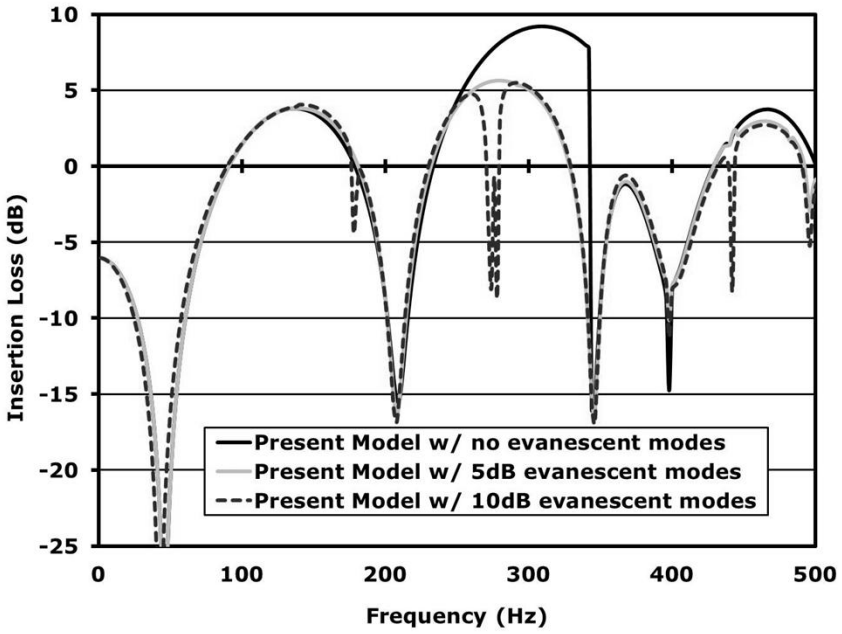


**Figure 4.2 – Effect of including evanescent modes**

## 4.2 Effect of Aperture Thickness

### 4.2.1 Low frequency effect of aperture thickness

Figures 4.3 and 4.4, large and small aperture, respectively, show the insertion loss for the present model for the dimensions presented in Table 3.1. Recall that in these models the aperture was not centered on the wall in order to excite all cavity modes in the frequency range of interest. The insertion loss was calculated from the ratio of the average acoustic energy density in the cavity and the average energy density of the incident plane wave, Equation (2.38). For both aperture cross-sections, insertion loss increased with increasing aperture thickness up until the (1,1) mode in the cavity at 321Hz. For frequencies above 321Hz, increasing the aperture thickness did not improve the insertion loss. At low frequencies, 3dB of insertion loss was gained by increasing the thickness of the large aperture from 0.03m to 0.2m as shown in Figure 4.3, and 8dB was gained in the case of the small aperture as shown in Figure 4.4. The abrupt drop in insertion loss at approximately 300Hz in Figures 4.3 and 4.4 is an artifact of keeping a finite number of evanescent modes in the calculation. (For the small aperture, this resulted in overestimating the insertion loss by more than 5dB, Figure 4.4.) At this particular drop, had the (1,1) cavity mode been included in calculations for a few frequencies below this dip, which indicates its introduction, the curve would be smoother.

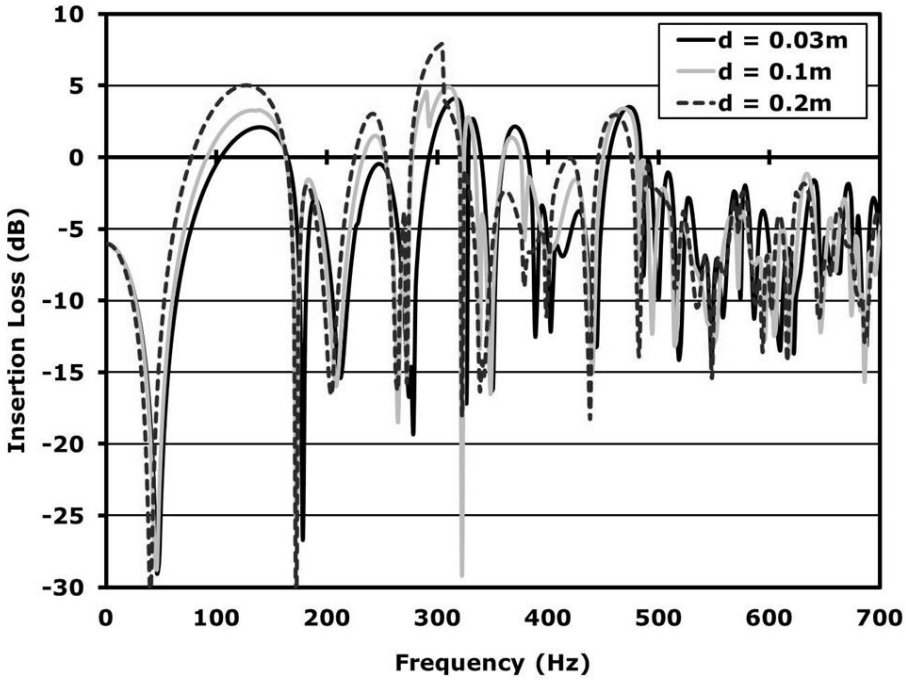


**Figure 4.3 – Insertion loss of present model with large aperture, effect of aperture thickness**

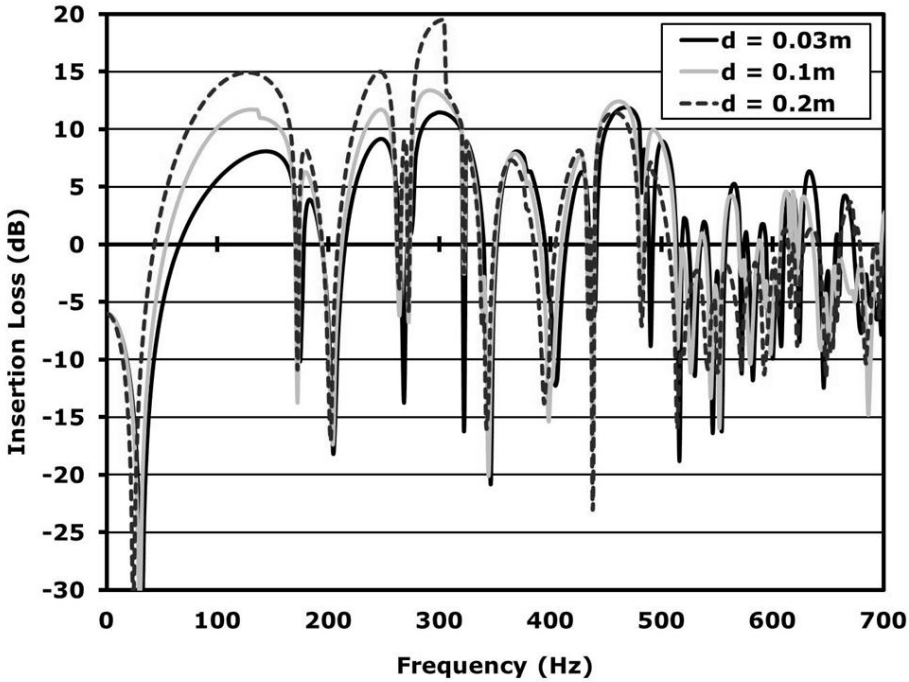


**Figure 4.4 – Insertion loss of present model with small aperture, effect of aperture thickness**

4.2.2 Broadband effect of aperture thickness

Figures 4.5 – 4.7 present the broadband frequency effect of the large aperture. First the insertion loss of the aperture bounded by half space on both sides was calculated for all three thicknesses using the method described in Sgard et al. (2007) (Figure 4.5). For the deep (0.2m) and medium (0.1m) thickness apertures, the insertion loss was highly dependent on the modes in the aperture; however, there was little variation in insertion loss for the thin (0.03m) aperture from 0Hz to 2kHz. The frequency response of the aperture alone was plotted with the response for the whole system, aperture backed by the cavity, for the deep and medium apertures in Figures 4.6 and 4.7, respectively. Notice that, particularly in Figure 4.6 which displays the effect of the thick aperture, the response of the aperture acts as a filter for the total response.

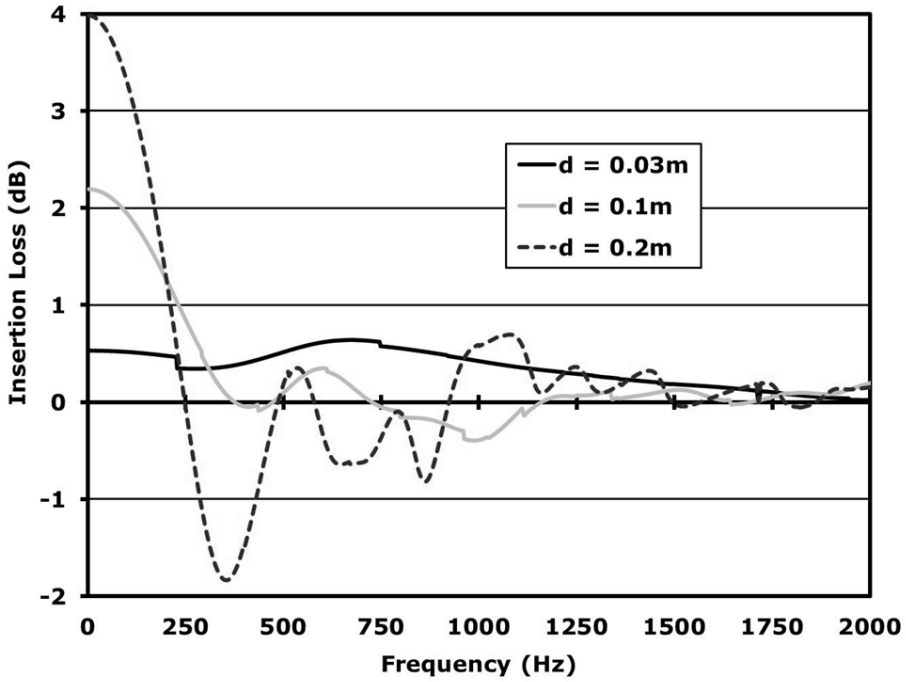


**Figure 4.5 – Insertion loss of large aperture bounded on both sides by half-space**

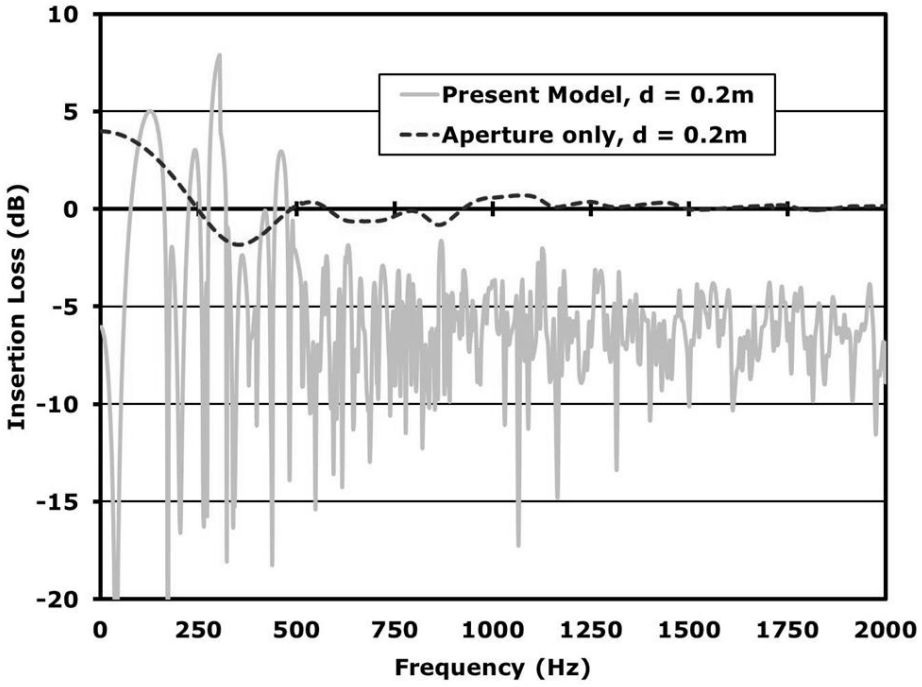


**Figure 4.6 – Comparison of present model and aperture only for large, deep aperture**

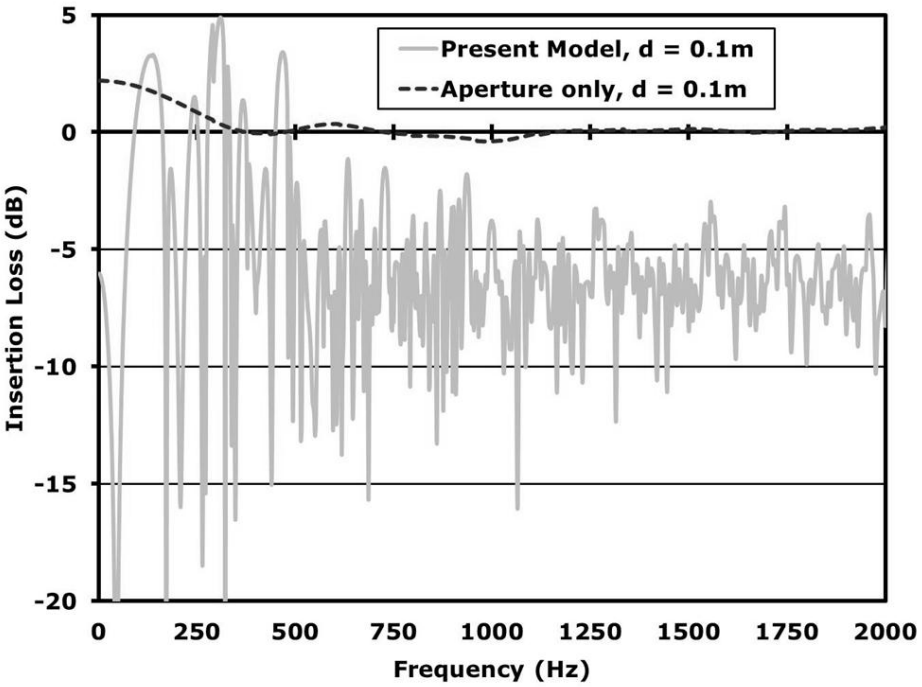


**Figure 4.7 – Comparison of present model and aperture only for large, medium aperture**

The broadband frequency response of the small apertures was also studied, and results are presented in Figures 4.8 – 4.10. First, using the procedure from Sgard et al. (2007), the insertion loss of the small apertures bounded by half space on both sides was calculated for all three thicknesses (Figure 4.8). As for the large aperture, the insertion loss of the deep (0.2m) and medium (0.1m) thickness apertures was highly dependent on the modes in the aperture, and there was little variation in insertion loss for the thin (0.03m) aperture from 0Hz to 2kHz. The frequency response of the aperture alone was plotted with the response for the whole system for the deep and medium apertures in Figures 4.9 and 4.10, respectively. The filtering effect of the small aperture was more defined than in the case of the large apertures, especially for the deep aperture (Figure 4.9).

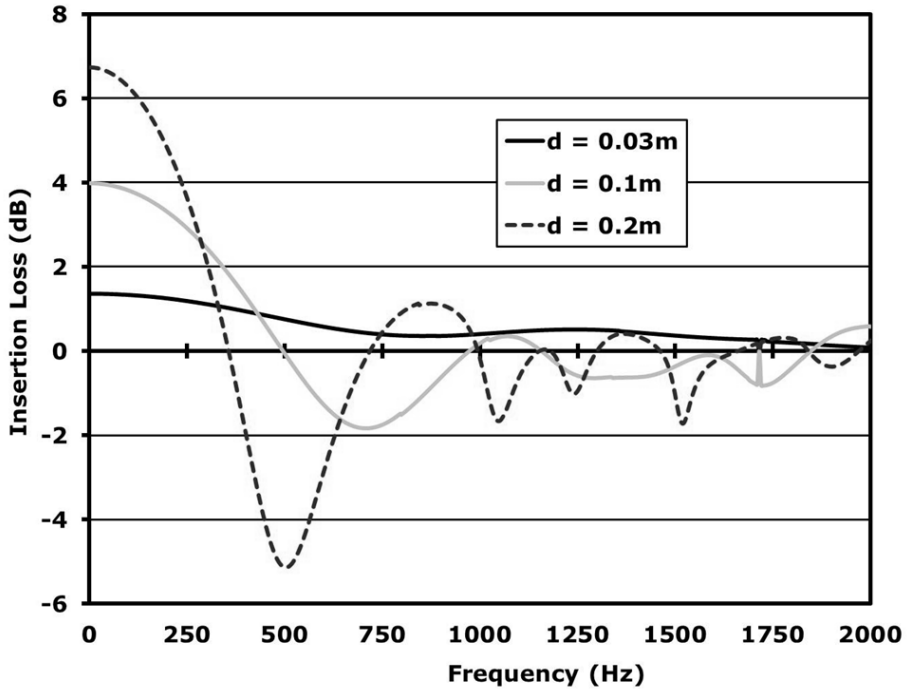


**Figure 4.8 – Insertion loss of small aperture bounded on both sides by half-space**

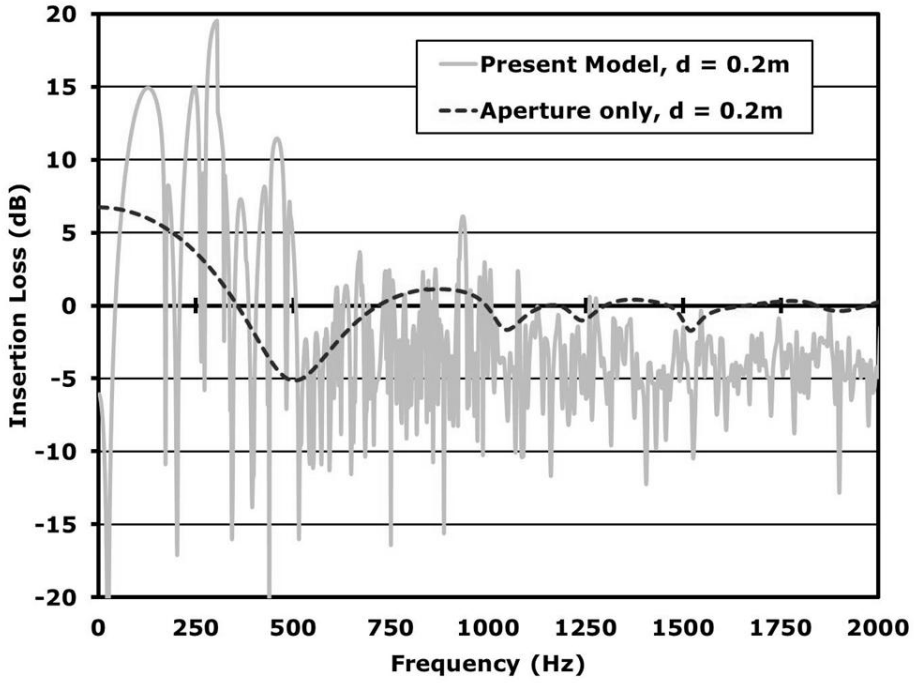


**Figure 4.9 – Comparison of present model and aperture only for small, deep aperture**

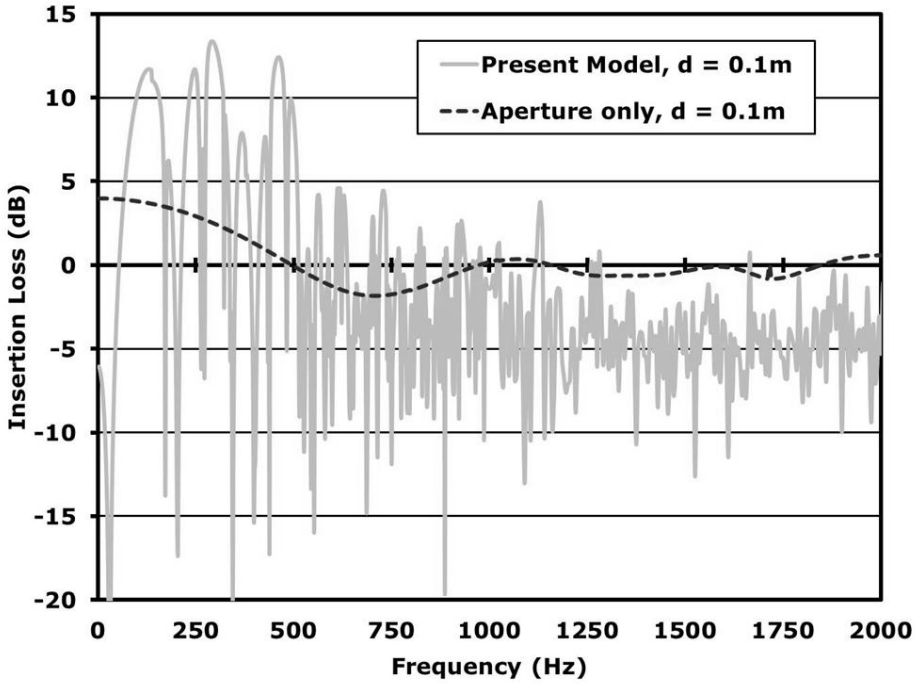


**Figure 4.10 – Comparison of present model and aperture only for small, medium aperture**

4.2.3 One-third octave band measurements and simulations

To determine the decrease in sound pressure level (SPL) that one might experience in the cavity due to increasing the thickness of the aperture, the SPL was measured and simulated at the four microphone positions listed in Table 3.3 for thin and deep apertures. Figures 4.11 – 4.14 present the difference in SPL at each microphone location for 1/3$^{rd}$ octave bands 63Hz to 4kHz as a result of increasing the aperture thickness. Positive values indicate that increasing the aperture thickness resulted in lower SPLs in the cavity. The results shown are the numerical average of the three SPLs measured for each aperture setting at each microphone location. As mentioned in Chapter 3, the system in the simulations was excited by a plane wave 45° from the plan and section planes; whereas, in the experiment, the excitation was based on the general response of the test room, which could be assumed to be diffuse above the Schroeder frequency, 217Hz. The averaged SPLs at the three microphones in the test room were within 4dB down to the 80Hz 1/3$^{rd}$ octave band other than in the 200Hz octave band in which averaged SPLs varied by as much as 6dB.

The measured and simulated results for the large aperture are presented in Figures 4.11 and 4.12, respectively. Except for the 160Hz band, the experiment and calculation had good agreement. Both show that the aperture thickness had a positive although decreasing effect moving from the 63Hz band to the 160Hz band and then had an increased effect in the 200Hz and 250Hz octave bands. As predicted by the insertion loss calculations, increasing the aperture thickness resulted in lower sound pressure level for frequencies below the (1,1) cavity mode, which occurs in the 315Hz band, and had little

effect at frequencies above this mode. The first asymmetric mode in the cavity occurs in the 160Hz mode. Notice in Figure 4.3, that due to the frequency resolution of the present model, the insertion loss of the deep aperture was 5dB less than was calculated for the other due to aperture thicknesses. The drastic difference in the experiment and simulation results in the 160Hz band can be attributed to aforementioned issue of numerical resolution and the difference in excitation. The measured results showed little change in SPL due to increasing aperture thickness in the 315Hz to 800Hz bands and slight decrease in SPL beginning in the 1kHz band, which is where higher order modes in the aperture appear.

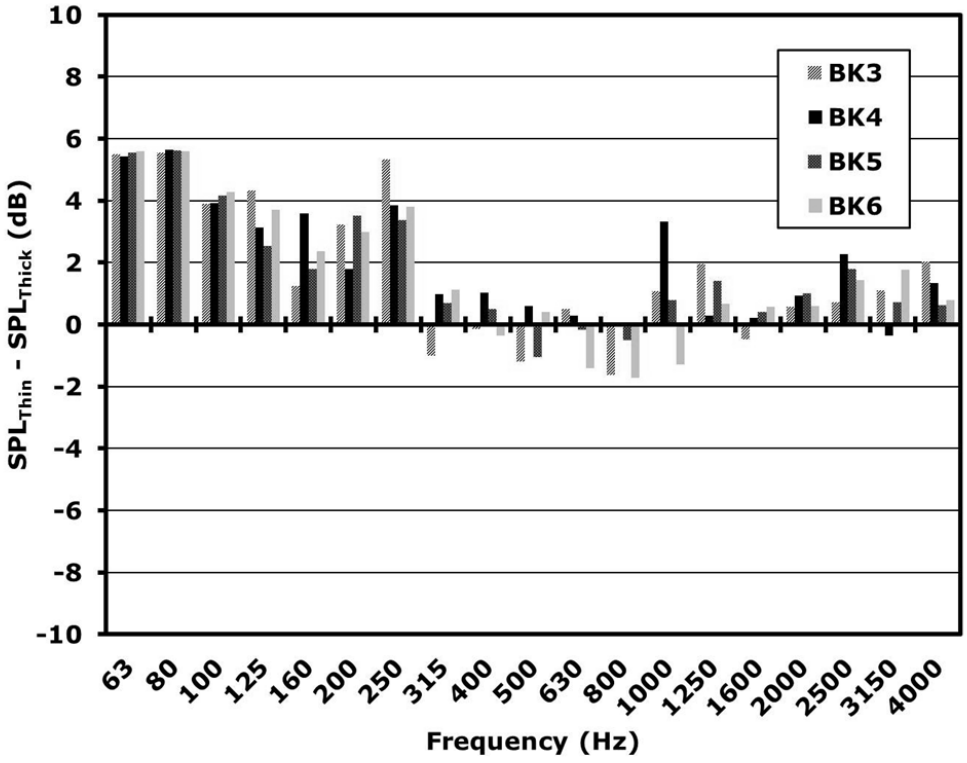


**Figure 4.11 – 1/3rd octave band difference in SPL for large aperture experiment**

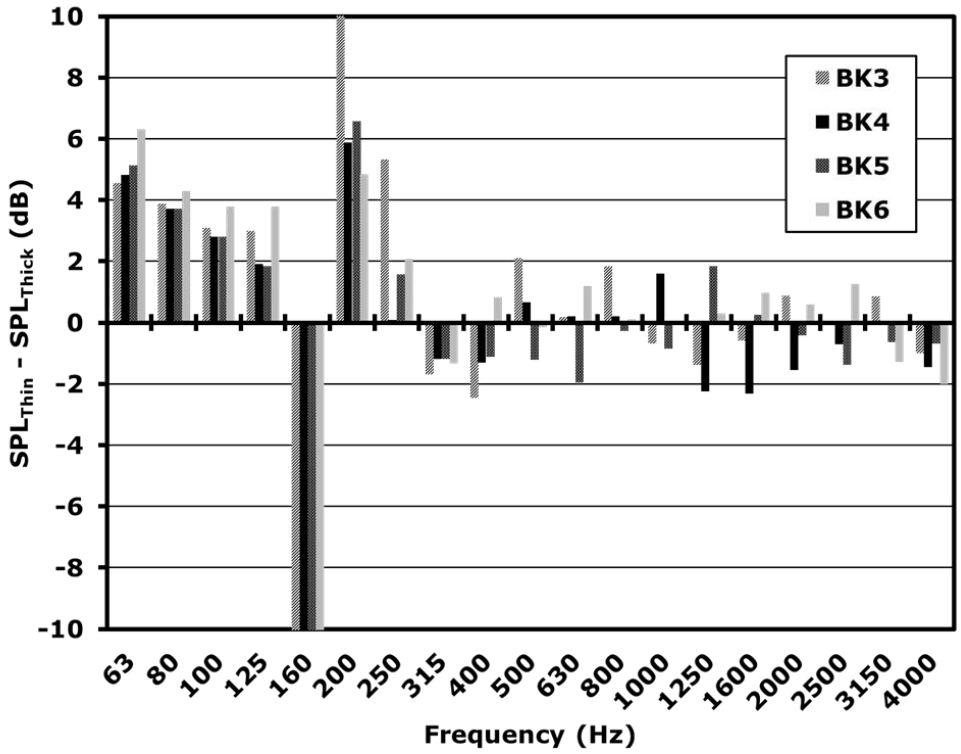


**Figure 4.12 – 1/3 octave band difference in SPL for large aperture calculation**

The measured and simulated results for the small aperture are presented in Figures 4.13 and 4.14, respectively. The experimental and simulated results also had good agreement. In the 160Hz band, the simulated effect was less than what was measured; although the difference was much less drastic than for the large aperture. This discrepancy was primarily due to not having identical sources for the experiment and simulation. Note in Figure 4.4 that the insertion loss at the (1,1) cavity mode was the same for the deep and small apertures, as opposed to the large aperture study. Both experiment and simulation showed that increasing the aperture thickness decreased the SPL in the cavity below the (1,1) mode and had less effect above this mode. The measured results for the small aperture, Figure 4.13, reveal the filtering effect of the

aperture as predicted in Figures 4.8 and 4.9. The minimum insertion loss for the small, deep aperture by itself (half-space on both sides, Figure 4.8) occurred near 500Hz and the second maximum around 800Hz. The dip is mimicked by the response in the 315Hz to 630Hz bands, and the second maximum in the 800Hz and 1kHz bands.

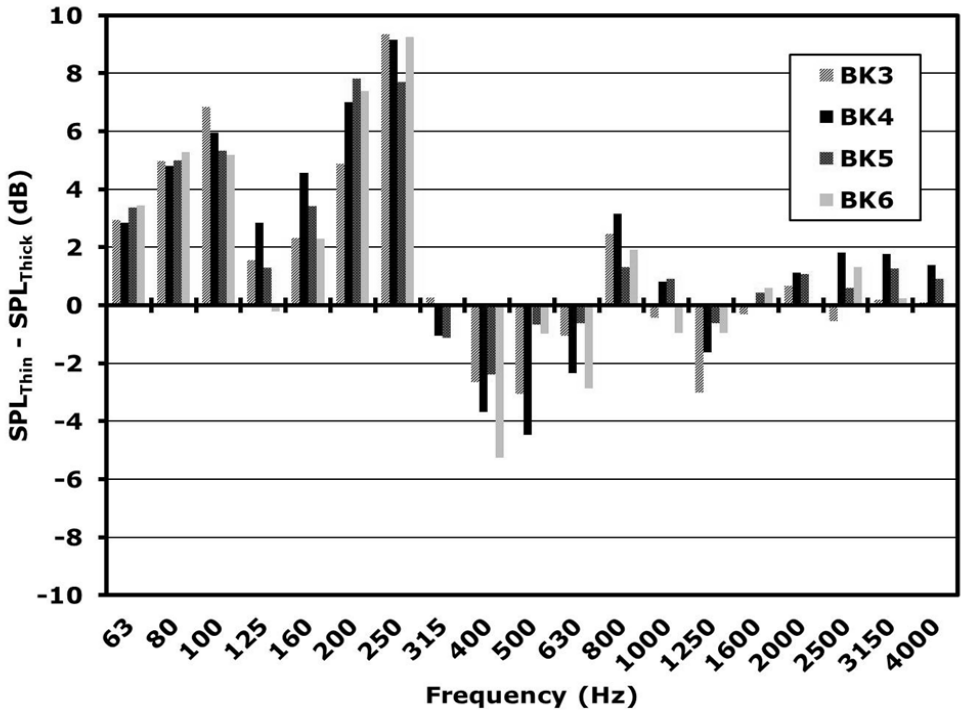


**Figure 4.13 – 1/3rd octave band difference in SPL for small aperture experiment**

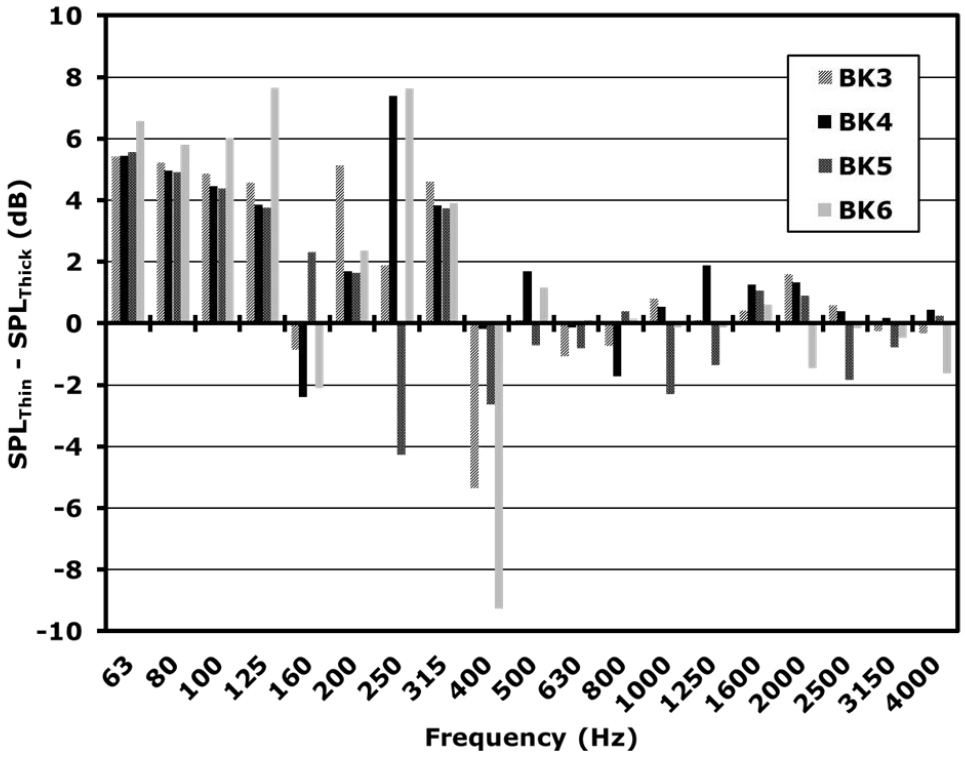


**Figure 4.14 – 1/3 octave band difference in SPL for small aperture calculation**

### 4.3 Summary

The analytical model developed in Chapter 2 was calculated numerically and was successfully verified at low frequencies by FEM. It was shown that including only a finite number of evanescent modes in the cavity and aperture in the calculation introduces irregularities. Broad frequency simulations showed that increasing the thickness of the aperture improved the insertion loss by up to 6dB but only for frequencies below the (1,1) cavity mode. This was also consistent with 1/3$^{rd}$ octave band measurements and calculations. Futhermore, the filtering of the aperture that appeared in the frequency response occurred in the measurement results as well and was particularly well defined for the small aperture.

# Chapter 5 – Extending Model to Impedance-Mobility Approach

## 5.1 Impedance-Mobility Approach

### 5.1.2 Introduction

The third goal of this work was to re-express the results of Chapter 2 in matrix form such that they could be used with the impedance-mobility approach to apply active noise control to a space. From just a simple computation standpoint, the impedance-mobility approach is beneficial because it reduces the large system of equations in Equation (2.33) to the manipulation of matrices a quarter of the size, many of which are diagonal matrices.

Frequencies of interest require the consideration of multiple modes in the aperture and cavity. The three regions (half-space, aperture, and cavity) cannot be simply represented with the long wavelength approximation as one dimensional circuit elements like a Helmholtz resonator, which can be represented as a series, mass-spring-damper circuit. (The Helmholtz resonance of the system is discussed in Section 4.1.1.) However, the elements can be considered in terms of complex acoustic or mechanical impedance matrices or complex mechanical mobility matrices (inverse of mechanical impedance). The mobility representation is useful when the source has a defined velocity or when one is interested in the vibration of an object (Lau and Tang, 2001; Kim and Brennan, 1999). There are only acoustic domains in this study, i.e. all rigid boundaries, so the following expressions will contain only acoustic and mechanical impedance, which are related by $Z^A = Z^M/A^2$.

5.1.2 Matrix representation of boundary equations

For this chapter, bold letters and square brackets represent matrices, regular print letters are vectors, and italicized letters are scalars. Equation (2.31) can be written in matrix form as in Equation (5.1), where **K** is a diagonal matrix containing the complex exponentials that define the propagation of each mode in the $+z$ direction at $z = 0$ in the aperture. **Γ** is the matrix of reflection coefficients at $z = d$ defined as $\mathrm{P_a^-} = \mathbf{\Gamma}\mathrm{P_a^+}$, where $\mathrm{P_a^+}$ and $\mathrm{P_a^-}$ are vectors containing the pressure amplitudes for each mode in the $+z$ and $-z$ directions, respectively. (In Chapter 2, acoustic pressure in the aperture and cavity was defined such that it had zero phase at the plane $z = d$.) $\mathbf{Z_a^A}$ is the diagonal matrix containing the characteristic acoustic impedance of each mode in the aperture, which in algebraic terms from Chapter 2 can be expressed as $Z^A_{a,mn} = \rho c_{a,mn}/A_a$.

$$A_a[\mathbf{K} + \mathbf{K}^{-1}\mathbf{\Gamma}]\mathrm{P_a^+} + \mathbf{Z_a^{M,rad}}\frac{1}{A_a}[\mathbf{Z_a^A}]^{-1}[\mathbf{K} - \mathbf{K}^{-1}\mathbf{\Gamma}]\mathrm{P_a^+} = \mathrm{F_{inc,a}} \tag{5.1}$$

All other notation is consistent with Chapter 2, although written in matrix or vector form rather than sums of modes. Superscripts imply impedance type, mechanical or acoustic, which are related by area squared $Z^A = Z^M/A^2$. Subscripts indicate whether the variable is in terms of aperture modes or cavity modes. For instance, $A_a$ is the scalar cross-sectional area of the aperture, $\mathrm{F_{inc,a}}$ is a vector of incident force values for each aperture mode as defined in Equation (2.19), and $\mathbf{Z_a^{M,rad}}$ is a square matrix of the mechanical radiation impedance as in Equation (2.20).

By using the property that a matrix multiplied by its inverse is the identity matrix, Equation (5.1) can be rewritten in terms of the particle velocity amplitudes at $z = 0$ as in Equation (5.2), where $\mathrm{U_a} = A_a^{-1}[\mathbf{Z_a^A}]^{-1}[\mathbf{K} - \mathbf{K}^{-1}\boldsymbol{\Gamma}]\mathrm{P_a^+}$ and $\mathbf{Z_a^M} = A_a^2\mathbf{Z_a^A}$.

$$[\mathbf{K} + \mathbf{K}^{-1}\boldsymbol{\Gamma}][\mathbf{K} - \mathbf{K}^{-1}\boldsymbol{\Gamma}]^{-1}\mathbf{Z_a^M}\mathrm{U_a} + \mathbf{Z_a^{M,rad}}\mathrm{U_a} = \mathrm{F_{inc,a}} \tag{5.2}$$

In the same manner, Equation (2.32) can be written in matrix form as in Equation (5.3), where $\mathbf{I}$ is the identity matrix. $\mathbf{Z_a^{A,c}}$ is the acoustic impedance of the cavity in terms of aperture modes. The reflection coefficient matrix $\boldsymbol{\Gamma}$ can now be solved for only in terms of impedances.

$$A_a[\mathbf{I} + \boldsymbol{\Gamma}]\mathrm{P_a^+} - A_a\mathbf{Z_a^{A,c}}[\mathbf{Z_a^A}]^{-1}[\mathbf{I} - \boldsymbol{\Gamma}]\mathrm{P_a^+} = 0 \tag{5.3}$$

$$\boldsymbol{\Gamma} = \left[\mathbf{Z_a^{A,c}}[\mathbf{Z_a^A}]^{-1} + \mathbf{I}\right]^{-1}\left[\mathbf{Z_a^{A,c}}[\mathbf{Z_a^A}]^{-1} - \mathbf{I}\right] \tag{5.4}$$

At the cut-on frequency for any particular mode in the cavity or aperture, the phase speed for that mode approaches infinity, which implies that $Z_{a,mn}^{A} \to \infty$ at cut-on in the aperture and $Z_{\xi\eta,mn}^{A,c} \to \infty$ at cut-on in the cavity. A quick analysis of the expression above for the reflection coefficient at $S_2$ reveals that it tends to -1 (pressure release) when the aperture is excited at a cut-on frequency, 1 (rigid boundary) for a cut-on frequency in the cavity, and 0 (no reflection) if modes in the aperture and cavity have the same cut-on frequency.

## 5.2 Input Impedance

### 5.2.1 Input impedance of load at the end of a transmission line

Figure 5.1 contains a simple electrical transmission line with a source voltage $\tilde{V}_g$, source impedance $Z_g$, transmission line characteristic impedance $Z_0$, and load impedance $Z_L$. The source sees the load impedance as translated along the transmission and in series with $Z_g$. This translated impedance is known as the input impedance, $Z_{in}$, which can be calculated using Equation (5.5), where $l$ is the length of the transmission line and $k = 2\pi/\lambda$ is the wavenumber in the transmission line. $Z_{in}$ is the ratio of total voltage to total current at the location $z = -l$ along the transmission line.

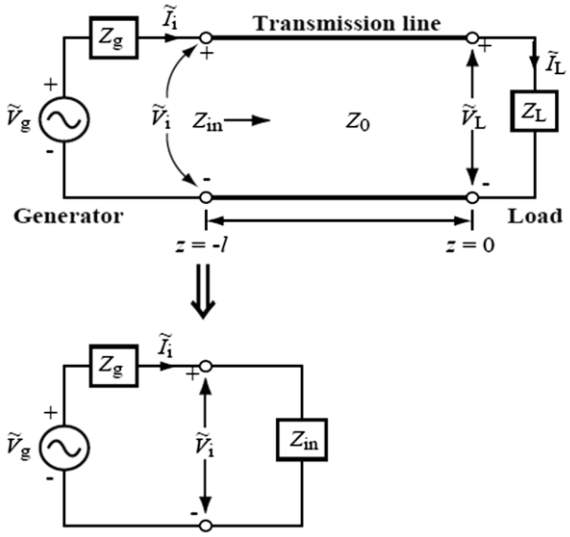


**Figure 5.1 - Example of replacing a load impedance at the end of a transmission line with an input impedance at near the source (Ulaby, 2006, p. 62)**

$$Z_{in} = Z_0 \frac{Z_L + jZ_0 \tan(kl)}{Z_0 + jZ_L \tan(kl)} \tag{5.5}$$

The reflection coefficient, or energy ratio of the wave traveling in the $-z$ direction to the wave traveling in the $+z$ direction, at $z = 0$ is $R = (Z_L/Z_0 - 1)/(Z_L/Z_0 + 1)$ in terms of the line impedance and load impedance. Now, $Z_{in}$ can be expressed in terms of $R$.

$$Z_{in} = Z_0 \frac{e^{jkl} + Re^{-jkl}}{e^{jkl} - Re^{-jkl}} \tag{5.6}$$

5.2.2 Input impedance in present model

Noting the similarities between Equation (5.6) and the left-most term in Equation (5.2), the input impedance at surface $S_1$, or impedance seen by the incident wave looking into the aperture backed the cavity, is expressed by Equation (5.7). Equation (5.8) demonstrates that the incident wave sees the series combination of the radiation impedance and the input impedance. The equations below are expressed in units of mechanical impedance simply due to convention (Sgard et al., 2007; Pierce et al., 2002; Nelisse et al., 1998), and could be easily converted to acoustic impedances or mechanical mobililties.

$$\mathbf{Z}_{\mathbf{in,a}}^{\mathbf{M,c}} = [\mathbf{K} + \mathbf{K}^{-1}\boldsymbol{\Gamma}][\mathbf{K} - \mathbf{K}^{-1}\boldsymbol{\Gamma}]^{-1}\mathbf{Z}_{\mathbf{a}}^{\mathbf{M}} \tag{5.7}$$

$$\mathbf{Z}_{\mathbf{in,a}}^{\mathbf{M,c}}\mathrm{U_a} + \mathbf{Z}_{\mathbf{a}}^{\mathbf{M,rad}}\mathrm{U_a} = \mathrm{F_{inc,a}} \tag{5.8}$$

5.2.3 Deriving the cavity impedance using input impedance approach

In Equation (5.3), $\mathbf{Z_a^{A,c}}$ was introduced as the matrix rendition of the acoustic cavity impedance as seen from the aperture as defined in Equation (2.30). The cavity can be considered a terminated waveguide. Therefore, the cavity impedance can be derived by simply mapping the back wall to the aperture, which is more concise than the derivation in Chapter 2. The reflection coefficient of a rigid wall is 1. Therefore from Equation (5.7), the cavity impedance in terms of cavity modes can be expressed as in Equation (5.9), where $\mathbf{K_c}$ is the diagonal matrix containing the propagation terms exp $(jk_{c,rs}L_z)$ and $\mathbf{Z_c^A}$ is the diagonal matrix of characteristic acoustic impedance in the cavity $\rho c_{c,rs}/A_c$, where $A_c$ is the cross-sectional area in the cavity. Both matrices on the right hand side of (5.10) are diagonal so their product can be easily calculated, which is expressed in Equation (5.11). Equation (5.11) now represents the acoustic impedance of the cavity as seen at the plane $z = d$ in terms of the cavity mode pairs $rs$.

$$\mathbf{Z_c^{A,c}} = [\mathbf{K_c} + \mathbf{K_c^{-1}}][\mathbf{K_c} - \mathbf{K_c^{-1}}]^{-1}\mathbf{Z_c^A} \tag{5.9}$$

$$\mathbf{Z_c^{A,c}} = \begin{bmatrix} \ddots & 0 & 0 \\ 0 & j\tan(k_{c,rs}L_z) & 0 \\ 0 & 0 & \ddots \end{bmatrix}^{-1} \mathbf{Z_c^A} \tag{5.10}$$

$$\mathbf{Z_c^{A,c}} = \begin{bmatrix} \ddots & 0 & 0 \\ 0 & \dfrac{\rho c_{c,rs}}{jA_c\tan(k_{c,rs}L_z)} & 0 \\ 0 & 0 & \ddots \end{bmatrix} \tag{5.11}$$

To convert Equation (5.11) to mechanical impedance at the boundary, it must be multiplied by something with units of $m^4$. Multiplying by the squared area $A_c^2$ keeps the

impedance in terms of cavity modes. However, multiplying the right side by $\mathbf{C}$ and the left side by $\mathbf{C^T}$ maps the impedance to the aperture, where $\mathbf{C}$ is the coupling coefficient defined in Equation (2.27) and $\mathbf{C^T}$ is its transpose given by Equation (2.28). Since the coupling coefficients have units of $m^2$, the expression given in Equation (5.12) is mechanical impedance and is the matrix expression of the cavity impedance given in Equation (2.30).

$$\mathbf{Z_a^{M,c}} = \mathbf{C}\mathbf{Z_c^{A,c}}\mathbf{C^T} = \mathbf{C}\begin{bmatrix} \ddots & 0 & 0 \\ 0 & \dfrac{\rho c_{c,rs}}{jA_c \tan\left(k_{c,rs}L_z\right)} & 0 \\ 0 & 0 & \ddots \end{bmatrix}\mathbf{C^T} \tag{5.12}$$

5.2.4 Solving for acoustic pressure

Using the input impedance method, the load on any source placed anywhere in the system can be determined; all impedances just need to be mapped to the source. A similar method was used by Doak (1973b) to determine sound fields inside and outside of a finite duct containing an arbitrary source distribution.

For the geometry under investigation, the reflection coefficient and input impedance were calculated from the point of view of the aperture because the source was being applied at $z = 0$, which made $P_a^+$ the logical choice to solve for first. Substituting pressure into Equation (5.8) for the particle, Equation (5.13) can be used to evaluate $P_a^+$ for any incident force. With $P_a^+$ solved for, all other acoustic variables in the system can be calculated. Equation (5.14) provides the relationship between $P_a^+$ and $P_c$, the pressure amplitudes in the cavity.

$$A_a^{-1}[\mathbf{Z_a^A}]^{-1}[\mathbf{K}-\mathbf{K}^{-1}\boldsymbol{\Gamma}]\mathrm{P_a^+} = \left[\mathbf{Z_{in,a}^{M,c}}+\mathbf{Z_{rad}^{M}}\right]^{-1}\mathrm{F_{inc,a}} \tag{5.13}$$

$$\mathbf{C}\begin{bmatrix}\ddots & 0 & 0\\ 0 & \cos\left(k_{c,rs}L_z\right) & 0\\ 0 & 0 & \ddots\end{bmatrix}\mathrm{P_c} = A_a[\mathbf{I}+\boldsymbol{\Gamma}]\mathrm{P_a^+} \tag{5.14}$$

### 5.3 Thin Aperture Limit

For an aperture thin enough such that $\exp\left(jk_{a,mn}d\right) \approx 1 + jk_{a,mn}d$ and wavelengths of interest short enough to excite multiple modes, the input impedance can be approximated by Equation (5.15), where $\left[jk_{a,m}d\right]$ is the diagonal matrix of propagation exponents. Equation (5.16) was obtained by using the relation in Equation (5.3).

$$\mathbf{Z_{in,a}^{M,c}} \approx \left[\mathbf{I}+\boldsymbol{\Gamma}+\left[jk_{a,m}d\right](\mathbf{I}-\boldsymbol{\Gamma})\right]\left[\mathbf{I}-\boldsymbol{\Gamma}+\left[jk_{a,m}d\right](\mathbf{I}+\boldsymbol{\Gamma})\right]^{-1}\mathbf{Z_a^M} \tag{5.15}$$

$$\mathbf{Z_{in,a}^{M,c}} \approx \left[\mathbf{Z_a^{M,c}}[\mathbf{Z_a^M}]^{-1}+\left[jk_{a,m}d\right]\right]\left[\mathbf{I}+\left[jk_{a,m}d\right]\mathbf{Z_a^{M,c}}[\mathbf{Z_a^M}]^{-1}\right]^{-1}\mathbf{Z_a^M} \tag{5.16}$$

Now, if the aperture is thin enough such that $\mathbf{I} \gg \left[jk_{a,m}d\right]\mathbf{Z_a^{M,c}}\text{-}[\mathbf{Z_a^M}]^{-1}$, then the input impedance becomes the series combination of cavity impedance and a positive imaginary term that represent the contribution of the mass of the fluid in the aperture.

$$\mathbf{Z_{in,a}^{M,c}} \approx \mathbf{Z_a^{M,c}} + \left[jk_{a,m}d\right]\mathbf{Z_a^M} \tag{5.17}$$

## 5.4 Summary

Frequencies of interest require the consideration of multiple modes in the aperture and cavity. Thus, the three regions cannot be simply represented by one dimensional circuit elements. However, the elements can be considered in terms of complex acoustic or mechanical impedance matrices or complex mechanical mobility matrices, which make them compatible with the impedance-mobility approach used in structural-acoustic interactions. Using the input impedance method, the load on any source placed within the system can be determined, and by extension, the fields everywhere. Future work may consider how to incorporate the effects of fully or partially open windows into active noise control systems using the impedance-mobility method. This approach also reduces the matrices to be solved to one fourth of the size of the matrices associated with the system of equations in Chapter 2, making the impedance-mobility approach potentially faster computationally.

## Chapter 6 – Conclusions

An analytical model of an aperture of finite thickness set in a rigid baffle and backed by a cavity was developed. Using Fourier expansions, the acoustic pressure in the aperture and cavity were modeled, and the half-space was modeled as the sum of incident and reflected plane waves and the wave radiated from the aperture.

The analytical model developed in Chapter 2 was implemented numerically and was successfully verified at low frequencies by FEM. An experiment was also performed wherein the aperture connected the cavity, all made from plywood, to a source room. It was shown that including only a finite number of evanescent modes in the cavity and aperture in the calculation introduces irregularities. Six apertures were used to study the effect of thickness on insertion loss. Apertures of three different depths were made for two aperture cross-sectional areas. Broad frequency simulations showed that increasing the thickness of the aperture improved the insertion loss up to 6dB for the small aperture and up to 4dB for the large aperture for frequencies below the (1,1) cavity mode. This was also consistent with $1/3^{rd}$ octave band measurements and calculations. Also, the filtering of the aperture that appeared in the frequency response occurred in the measurement results as well and was particularly well-defined for the small aperture.

Therefore as the cross-sectional area of the aperture approaches that of the cavity, the aperture thickness has less effect. For the aperture-cavity systems analyzed, the (1,1) mode of the cavity appeared to be a significant limit on the effect of thickness. However, this may just be a coincidence of the geometries chosen. The simulated and experimental

models were created at one-fifth scale. Therefore, much of the benefit seen by simply increasing the thickness would occur below 50Hz in full scale.

Frequencies of interest require the consideration of multiple modes in the aperture and cavity. Thus, the three regions cannot be simply represented by one dimensional circuit elements. However, the elements can be considered in terms of complex acoustic or mechanical impedance matrices or complex mechanical mobility matrices, which make them compatible with the impedance-mobility approach used in structural-acoustic interactions. This approach also reduces the matrices to be solved to one fourth of the size of the matrices associated with the system of equations in Chapter 2, making the impedance-mobility approach potentially faster computationally. Using the input impedance method, the load on any source placed within the system can be determined, and therefore, the fields everywhere as well. This development is the primary significance of this work. Now, future work may consider how to incorporate the effects of fully or partially open windows into active noise control systems using the impedance-mobility method.

## References

Amundsen, A. H., Klaeboe, R., and Aasvang, G. M. (**2013**). "Long-term effects of noise reduction measures on noise annoyance and sleep disturbance: The Norwegian facade insulation study," The Journal of the Acoustical Society of America, **133**, 3921–3928. doi:10.1121/1.4802824

De Araújo, B., and Bistafa, S. (**2012**). "Façade elements for natural ventilation and sound insulation," Building Acoustics, **19**, 25–44. doi:10.1260/1351-010X.19.1.25

Asakura, T., Miyajima, T., and Sakamoto, S. (**2013**). "Prediction method for sound from passing vehicle transmitted through building façade," Applied Acoustics, **74**, 758–769. doi:10.1016/j.apacoust.2012.11.011

Berardi, U. (**2012**). "A comparison of measurement standard methods for the sound insulation of building façades," Building Acoustics, **19**, 267–282. doi:10.1260/1351-010X.19.4.267

Bies, D. A., and Hansen, C. H. (**2009**). *Engineering Noise Control: Theory and Pratice*, Taylor & Francis, 768 pages.

Buratti, C., Barelli, L., and Moretti, E. (**2013**). "Wooden windows: Sound insulation evaluation by means of artificial neural networks," Applied Acoustics, **74**, 740–745. doi:10.1016/j.apacoust.2012.12.001

Doak, P. E. (**1973**). "Excitation, transmission and radiation of sound from source distributions in hard-walled ducts of finite length (I): The effects of duct cross-

section geometry and source distribution space-time pattern," Journal of Sound and Vibration, **31**, 1–72. doi:10.1016/S0022-460X(73)80249-4

Doak, P. E. (**1973**). "Excitation, transmission and radiation of sound from source distributions in hard-walled ducts of finite length (II): The effects of duct length," Journal of Sound and Vibration, **31**, 137–174. doi:10.1016/S0022-460X(73)80372-4

Duhamel, D., and Sergent, P. (**1998**). "Active noise control of an incoherent line source," Journal of Sound and Vibration, **212**, 141–164. doi:06/jsvi.1997.1454

Emms, G. W., and Fox, C. (**2001**). "Control of sound transmission through an aperture using active sound absorption techniques: a theoretical investigation," Applied Acoustics, **62**, 735–747. doi:doi: DOI: 10.1016/S0003-682X(00)00063-3

Gardonio, P., and Brennan, M. J. (**2002**). "On the origins and development of mobility and impedance methods in structural dynamics," Journal of Sound and Vibration, **249**, 557–573. doi:10.1006/jsvi.2001.3879

Herrin, D. W., and Seybert, A. F. (**2006**). "RP-1218 -- Numerical methods for low-frequency HVAC noise applications".

Horner, J. L., and Peat, K. S. (**2006**). "Approximations for the scattered field potential from higher mode transmission in rectangular apertures," J. Acoust. Soc. Am., **119**, 3568–3576. doi:10.1121/1.2197792

Hu, S., Rajamani, R., and Yu, X. (**2013**). "Directional cancellation of acoustic noise for home window applications," Applied Acoustics, **74**, 467–477. doi:10.1016/j.apacoust.2012.08.004

Ishizuka, T., and Fujiwara, K. (**2012**). "Traffic noise reduction at balconies on a high-rise building fa[c-cedilla]ade," The Journal of the Acoustical Society of America, **131**, 2110–2117. doi:10.1121/1.3682052

Jean, P. (**2009**). "Sound transmission through opened windows," Applied Acoustics, **70**, 41–49. doi:10.1016/j.apacoust.2008.01.007

Kim, S. M., and Brennan, M. J. (**1999**). "A compact matrix formulation using the impedance and mobility approach for the analysis of structural-acoustic systems," Journal of Sound and Vibration, **223**, 97–113. doi:10.1006/jsvi.1998.2096

Kinsler, L. E., Frey, A. R., Coppens, A. B., and Sanders, J. V. (**2000**). *Fundamentals of Acoustics*, John Wiley & Sons, Inc., 4th ed., 560 pages.

Kluizenaar, Y. de, Salomons, E. M., Janssen, S. A., Lenthe, F. J. van, Vos, H., Zhou, H., Miedema, H. M. E., et al. (**2011**). "Urban road traffic noise and annoyance: The effect of a quiet fa[c-cedilla]ade," The Journal of the Acoustical Society of America, **130**, 1936–1942. doi:10.1121/1.3621180

Kropp, W., and Berillon, J. (**1998**). "A theoretical model to investigate the acoustic performance of building facades in the low and middle frequency range," Acta Acustica, **84**, 681–688.

Kwon, B., and Park, Y. (**2013**). "Interior noise control with an active window system," Applied Acoustics, **74**, 647–652. doi:10.1016/j.apacoust.2012.11.005

Lau, S. (**2003**). *Active Control of Sound Transmission into Enclosure Through a Panel* (Doctor of Philosophy), Hong Kong Polytechnic University, Hong Kong, 313 pages.

Lau, S. K., and Tang, S. K. (**2001**). "Sound fields in a rectangular enclosure under active sound transmission control," J. Acoust. Soc. Am., **110**, 925–938. doi:10.1121/1.1387095

Muehleisen, R. T. (**1996**). *Reflection, Radiation, and Coupling of Higher Order Modes at Discontinuities in Finite Length Rigid Walled Rectangular Ducts* (Doctor of Philosophy), The Pennsylvania State University.

Naish, D. A., Tan, A. C. C., and Nur Demirbilek, F. (**2012**). "Estimating health related costs and savings from balcony acoustic design for road traffic noise," Applied Acoustics, **73**, 497–507. doi:10.1016/j.apacoust.2011.12.005

Nelisse, H., Beslin, O., and Nicolas, J. (**1998**). "A generalized approach for the acoustic radiation from a baffled or unbaffled plate with arbitrary boundary conditions, immersed in a light or heavy fluid," Journal of Sound and Vibration, **211**, 207–225. doi:10.1006/jsvi.1997.1359

Park, H. H., and Eom, H. J. (**1997**). "Acoustic scattering from a rectangular aperture in a thick hard screen," J. Acoust. Soc. Am., **101**, 595–598. doi:10.1121/1.417971

Pierce, A. D., Cleveland, R. O., and Zampolli, M. (**2002**). "Radiation impedance matrices for rectangular interfaces within rigid baffles: Calculation methodology and applications," J. Acoust. Soc. Am., **111**, 672–684. doi:10.1121/1.1430684

Sánchez Bote, J. L., Pedrero González, A., and Gómez Alfageme, J. J. (**2012**). "Procedure for verification of sound source coverage over façades according to the International Standard ISO 140–5," Applied Acoustics, **73**, 977–985. doi:10.1016/j.apacoust.2012.04.007

Sauter, Jr., A., and Soroka, W. W. (**1970**). "Sound transmission through rectangular slots of finite depth between reverberant rooms," J. Acoust. Soc. Am., **47**, 5–11. doi:10.1121/1.1911442

Sgard, F., Nelisse, H., and Atalla, N. (**2007**). "On the modeling of the diffuse field sound transmission loss of finite thickness apertures," J. Acoust. Soc. Am., **122**, 302–313. doi:10.1121/1.2735109

Sieck, C., and Lau, S.-K. (**2011**). "Noise propagation through open windows of finite depth into an enclosure," Proceedings of Meetings on Acoustics, **11**, 040004. doi:10.1121/1.3567154

Steele, C. (**2001**). "A critical review of some traffic noise prediction models," Applied Acoustics, **62**, 271–287. doi:10.1016/S0003-682X(00)00030-X

Trompette, N., Barbry, J.-L., Sgard, F., and Nelisse, H. (**2009**). "Sound transmission loss of rectangular and slit-shaped apertures: Experimental results and correlation with a modal model," J. Acoust. Soc. Am., **125**, 31–41. doi:10.1121/1.3003084

Ulaby, F. T. (**2006**). *Fundamentals of Applied Electromagnetics*, Prentice Hall, 5th ed.

Zhang, J., Jiang, W., and Li, N. (**2002**). "Theoretical and experimental investigations on coherence of traffic noise transmission through an open window into a rectangular room in high-rise buildings," J. Acoust. Soc. Am., **112**, 1482–1495. doi:10.1121/1.1488653